The mechanisms of jetting, vortex sheet and vortex ring development in asymmetric bubble dynamics

Yu, You; Smith, Warren; Wang, Qianxi; Leighton, Timothy G.

The mechanisms of jetting, vortex sheet and vortex ring development in asymmetric bubble dynamics

You Yu (于游),[1] Jie Cui (崔杰)*,[2] Warren R. Smith,[1] Qianxi Wang (汪前喜)*,[1] and Timothy G. Leighton[3]
[1)] *School of Mathematics, University of Birmingham, Edgbaston, Birmingham B15 2TT, UK*
[2)] *School of Naval Architecture and Ocean Engineering, Jiangsu University of Science and Technology, Zhenjiang, 212003, China*
[3)] *Institute of Sound and Vibration Research, University of Southampton, Southampton SO17 1BJ, UK*

(*Electronic mail: cuijie2006@hotmail.com; q.x.wang@bham.ac.uk)

(Dated: 12 November 2023)

Bubble dynamics near a rigid boundary at Reynolds numbers of O(10-100) exhibit significant viscous effect, associated with ultrasonic cavitation and cavitation damage. We study this phenomenon experimentally using high-speed photography of spark-generated bubble oscillation in silicone oils, whose viscosity is about three orders larger than water. Comparing to bubbles in water, bubble surfaces in silicone oil are more stable and thus more cycles of oscillations may be observed and studied. Additionally, we investigate this phenomenon numerically using the volume of fluid method. We propose a non-reflective boundary condition, reducing the computational domain's dimensions tenfold based on the far-field asymptotic behavior. This paper pays particular attention in the mechanism for the bubble jetting, the vortex sheet and the vortex ring development. Initially, a stagnation point at the bubble center moves away from the wall owing to asymmetric bubble expansion, leaving the bubble around the moment the bubble reaches its maximum volume. During this process, a vortex sheet forms inside the bubble. As the vortex sheet approaches the bubble interface, it transfers momentum to the gas-liquid interface, influencing the flow near the bubble wall. The high-pressure zone at the stagnation point drives the distal bubble surface to collapse first and fastest subsequently. This asymmetric collapse generates circulation around the bubble's side cross-section, leading to the development of a vortex ring within the bubble gas at the outer rim of the decaying vortex sheet. The vortex ring, with its core inside the bubble gas, functions like a bearing system in accelerating the jet.

I. INTRODUCTION

In this work, we study viscous bubble dynamics for a Reynolds number of O(10-100) as it relates to the start of a cavitation collapse, in order to identify the cause of the indentation in the bubble wall from which the later, high-speed and inertia-controlled jetting process grow. Viscous effects are essential for cavitation bubbles, whose population comprise mainly very small bubbles. The experimental studies for the bubble distributions of various cavitation structures (bubble filaments, bubble clusters and the acoustically cavitated jets) have shown a centroid at approximately an equilibrium radius of 2-4 μm[1]. Hydrodynamic cavitation is associated with wide and important applications, including damage to pumps, turbines, and propellers[2–5]. Acoustic cavitation also has applications in biomedical ultrasound[6–11], sonochemistry[12] and cavitation cleaning[13–16].

Experimental studies of collapsing bubbles capable of eroding metal have been largely focused on bubbles with radii $O(100)$ μm or larger with $Re = O(10^3)$ or larger[17–33]. Although other options are available[34,35], bubble dynamics are widely modeled using the boundary integral method based on potential flow theory[36–47]. Viscous bubble dynamics have also been simulated successfully based on the Navier–Stokes equations coupled with various interface-capturing schemes[48–59]. These computations are for $Re = O(10^3)$ or larger.

It is well known that the chemical consequences of cavitation are essentially determined by the conditions inside a collapsing bubble[60,61]. This collapse will not only occur at rigid boundaries but also when two bubbles are in close proximity in the cloud[62]. Our research will accurately simulate the fluid mechanics of the bubble gas during the asymmetric collapse.

We perform both experiments and computations for bubble dynamics. Experimental studies provide direct observation of bubble oscillation. Computations provide the detail on the generation and the evolution of the vortex sheet, the vortex ring, the flow field, the shockwave propagation, the jet development and impact on the rigid boundary, and the shear stress at the rigid boundary.

We conduct experiments for electric spark-generated bubbles in silicone oils with a high-speed camera. The use of spark-generated bubbles in water to study non-spherical bubble collapse, and the formation of jets is a well-established technique, in almost continuous use in research of this phenomenon from the 1980s[63] to recent years[64–68]. Ohl et al.[69] provides an excellent review. The hardware deployed in this research is substantially similar to that used in many water-based studies, but with the difference that the sparks are generated in silicone oil, not water[70]. This is because the viscosity of silicone oils are two to three orders larger than that of water. To perform experiments at the same Reynolds number for the processes that occur at the start of the collapse when the indentation forms, bubble size in silicone oils are two to three orders larger than that in water. More specifically, to carry out experiments for bubbles with $Re = O$(10-100) in water, bubbles radii are O(1-10) μm. The dynamics of microbubbles poses technical challenges owing to the high spatial and temporal resolution requirements. To carry out experiments for bubbles with $Re = O(10\text{-}100)$ in silicone oils, bubbles radii are $O(1\text{-}10)$ mm. Another advantage of using a high-viscosity liquid is that bubble surfaces in water often become unstable after the first cycle of oscillation. Bubble surfaces in silicone oil are more stable, and thus, more cycles of oscillations may be observed and studied.

Our numerical simulations are based on the compressible Navier-Stokes equations using OpenFOAM[71], following Koch et al.[51], Lechner et al.[53,54] and Zeng et al.[57]. One of the challenges in the computations is associated with the requirement for a large computational domain. To prevent the reflection from the far field, its typical dimension is on the order of $O(100R_{max})$, where R_{max} represents the maximum bubble radius. Another challenge is that the mesh and temporal resolution must be fine enough across the entire computational domain to model shockwave propagation accurately. The loss of energy associated with the emission of shockwaves at the end of the collapse was not accurately captured in the previous computations. This could be due to the mesh size not being fine enough for simulating the radiation of shockwaves. In order to circumvent this issue, a portion of the bubble's potential energy was manually removed at the end of the first cycle of oscillation to continue the computations and to achieve agreement with experiments for the second cycle[57]. Therefore, any development in the numerical model that can reduce the computational cost is highly desirable.

To resolve the aforementioned two problems, a non-reflective boundary condition is proposed based on the far-field asymptotic behavior, which is obtained from the weakly compressible theory[37,39,40]. This reduces the dimension of the computational domain tenfold. With this reduction in domain size, a sufficiently fine grid can be used for the computational domain to capture the shockwaves' radiation accurately. Our simulated bubble dynamics agree very well with experiments for both the first and second cycles of oscillation without manually adjusting the potential energy at the end of the first collapse.

We further study viscous bubble dynamics near a flat rigid boundary with $Re = O(10\text{-}100)$ and compare the results with that for $Re = O(10^3)$, in terms of bubble evolution, jet development, shockwave propagation, and the shear stress on the rigid boundary. In particular, we reveal that the vortex ring associated with a toroidal bubble is not generated instantaneously as the liquid jet penetrates the bubble but converts from a vortex sheet within the bubble gas during the later stages of expansion and subsequently develops.

The remainder of the paper is organized as follows: Section II details the experimental setup and numerical model. In section III, experimental results are presented for oscillations of both spherical and non-spherical bubbles. Numerical studies are further performed for bubble dynamics near a rigid boundary in section IV, which correlates well with experimental data, and viscous effects on bubble dynamics are discussed. Finally, the conclusions of the study are given in section V.

II. METHODOLOGY

In this section, we describe both the experiment setup and the computational model. The experiment uses a high-speed camera for electric spark-generated bubbles in silicone oils. The computational model is based on the volume of fluid method for two-phase viscous compressible flows.

A. Experiment

The experiment is carried out for electric spark-generated bubbles in silicone oils. Figure 1(a) illustrates the experimental setup used to generate a cavitation bubble and record its dynamics. The experiment is performed in a cubic acrylic container (0.3 m $\times$ 0.3 m $\times$ 0.6 m) filled with the liquid (water or silicone oils) to a depth of 0.2 m. The container is illuminated by a 2 kW LED non-strobe lamp positioned on the opposite side of the camera, passing through a white frosted glass film and a soft light plate. This arrangement allows for a more uniform projection of the light source. The images of the cavitation bubble are captured by a VRI-Phantom V611 high-speed camera working at 7900 frames per second (FPS) for 1280 Œ 800 resolution.

As shown in figure 1(b), the bubble is generated by an electric spark device. It comprises a 205 V DC power supply, a 1 kΩ resistor, a 6600 μF capacitor, and overlapping electrodes made of copper alloy. As mentioned in Cui et al.[32], electrodes extending from the capacitor poles are crossed and touched at their other ends in the liquid. Upon activating switch K1, the power supply converts 220 V AC into 205 V DC and the capacitor is charged to 205 V. This discharges the electronic energy instantaneously, leading to heating at the cross point, bubble generation, and simultaneous activation of the information acquisition button on the high-speed camera. The copper alloy wires, with a thin radius of 0.1 mm compared to the bubble radius of approximately 15 mm, are anticipated to have a minimal impact on the bubble dynamics.

Figure 2 shows the configuration of a bubble in the container in the experiment. The dimensionless standoff distance γ is defined as D/R_{max}, where D is the distance from the center of the initial bubble to the bottom of the container and R_{max} is the maximum bubble radius attained in the experiment. As the bubble is about $7R_{max}$ -$10R_{max}$ from the side walls of the container and the free surface, their effects on bubble dynamics are assumed to be negligible as the amplitude for the spherically symmetric shockwaves emitted by the bubble depends on the reciprocal of the distance traveled.

We choose the length scale R_{max} and the pressure scale $p_\infty - p_v$, where p_∞ is the hydrostatic pressure of the liquid, and p_v is the partial pressure of vapor inside the bubble. The Reynolds number and the Weber number of the bubble are defined as

$$Re = \frac{R_{max}\sqrt{\rho_\infty (p_\infty - p_v)}}{\mu_l}, We = \frac{R_{max}(p_\infty - p_v)}{\sigma}, \quad (1)$$

where ρ_∞ is the undisturbed density, μ_l is the dynamics viscosity, and σ is the surface tension coefficient of the liquid.

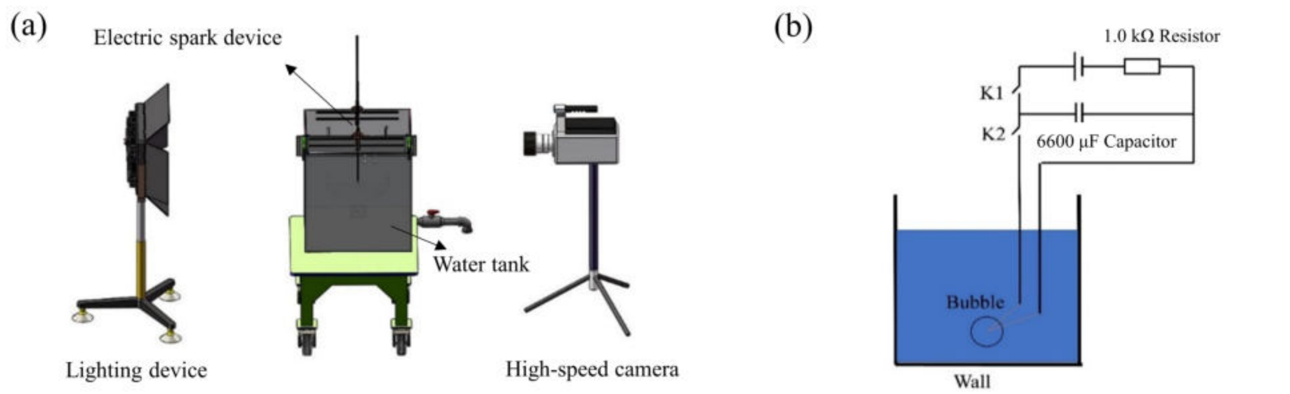

FIG. 1. (a) Experimental setup used to generate a cavitation bubble and record its dynamics. (b) Underwater discharge circuit, which is comprised of a 205 V DC power supply, a 1 kΩ resistor, a 6600 μF capacitor, and overlapping electrodes made of copper alloy.

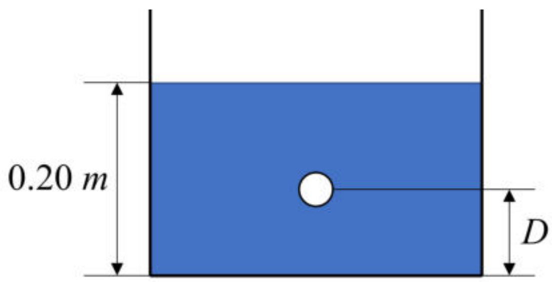

FIG. 2. Sketch of the bubble in a container filled with the liquid to a depth of 0.2 m in the experiment. D is the distance from the center of the initial bubble to the bottom of the container.

B. Numerical Simulation

In this subsection, the numerical model is described based on the compressible Navier-Stokes equations and the volume of fluid method[47,57–59,72–76]. A non-reflective boundary condition is proposed based on the asymptotic behavior, which reduces the dimension of the computational domain tenfold.

1. Numerical model

a. Equations of motion. In the volume of fluid (VOF) method, the two-phase flow of liquid and gas is treated as a "single-phase" flow. The fluid density ρ and viscosity μ are expressed in terms of the volume fraction parameter α of the liquid

$$\rho = \alpha\rho_l + (1-\alpha)\rho_g, \mu = \alpha\mu_l + (1-\alpha)\mu_g, \tag{2}$$

where the subscripts g and l denote the gas phase and the liquid phase, respectively. Equation (2) takes account of the volume fractions for liquid and gas being α and $1-\alpha$, and is the statistically correct for the two-phase flow.

The "single-phase" flow is thus governed by the compressible Navier–Stokes equations

$$\frac{\partial \rho}{\partial t} + \nabla\cdot(\rho\mathbf{u}) = 0, \tag{3}$$

$$\frac{\partial(\rho\mathbf{u})}{\partial t} + \nabla\cdot(\rho\mathbf{u}\mathbf{u}) = -\nabla p + \nabla\cdot\tau + \mathbf{f}_{st}, \tag{4}$$

where t is the time, $\mathbf{u}$ is the velocity field, p is the pressure, $\tau = \mu\left(\nabla\mathbf{u} + \nabla\mathbf{u}^T - \frac{2}{3}(\nabla\cdot\mathbf{u})\mathbf{I}\right)$ is the stress tensor with the unit tensor $\mathbf{I}$ and $\mathbf{f}_{st}$ represents the surface tension force acting at the interface of two fluids. It is treated as an external force for the "single-phase" flow acting at the interface, given as follows[77],

$$\mathbf{f}_{st} = \sigma\kappa\nabla\alpha, \tag{5}$$

where $\kappa = -\nabla\cdot\mathbf{n}$ is the curvature at the interface and $\mathbf{n} = \nabla\alpha/|\nabla\alpha|$ is the unit normal to the interface.

Assuming no mass transfer between the two fluids, the mass conservation can be expressed as a continuity equation for each phase. For the liquid phase, it can be expressed as

$$\frac{\partial(\alpha\rho_l)}{\partial t} + \nabla\cdot(\alpha\rho_l\mathbf{u}) = 0. \tag{6}$$

This can be written as

$$\frac{\partial\alpha}{\partial t} + \nabla\cdot(\alpha\mathbf{u}) = -\frac{\alpha}{\rho_l}\psi_l\frac{dp}{dt}, \tag{7}$$

where d/dt is the Lagrangian derivative, $\psi_l = d\rho_l/dp$ is the compressibility of the liquid calculated from the equation of state.

Similarly, the mass conservation for the gas phase can be written as

$$\frac{\partial(1-\alpha)}{\partial t} + \nabla\cdot((1-\alpha)\mathbf{u}) = -\frac{1-\alpha}{\rho_g}\psi_g\frac{dp}{dt}, \tag{8}$$

where $\psi_g = d\rho_g/dp$ is the compressibility of the gas. Combining equations (7) and (8) yields

$$\nabla\cdot\mathbf{u} = -\left(\frac{\alpha}{\rho_l}\psi_l + \frac{1-\alpha}{\rho_g}\psi_g\right)\frac{dp}{dt}. \tag{9}$$

Combining equations (7) and (9) gives us

$$\frac{\partial \alpha}{\partial t}+\nabla\cdot(\alpha\mathbf{u})=\alpha(1-\alpha)\left(\frac{\psi_g}{\rho_g}-\frac{\psi_l}{\rho_l}\right)\frac{dp}{dt}+\alpha\nabla\cdot\mathbf{u}. \quad (10)$$

To avoid numerical dissipation and retain the sharpness of the interface, an artificial "interface compression" term $\nabla\cdot(\alpha(1-\alpha)\mathbf{u}_c)$ is added to the equation, where $\mathbf{u}_c=|\mathbf{u}|\mathbf{n}$ is the compression velocity

$$\frac{\partial \alpha}{\partial t}+\nabla\cdot(\alpha\mathbf{u})+\nabla\cdot(\alpha(1-\alpha)\mathbf{u}_c)=\alpha(1-\alpha)\left(\frac{\psi_g}{\rho_g}-\frac{\psi_l}{\rho_l}\right)\frac{dp}{dt}+\alpha\nabla\cdot\mathbf{u}, \quad (11)$$

which is the transport equation of the volume fraction α determining the transient bubble surface[51,57–59,78].

The Tait equation[79] is adopted for the liquid phase

$$\rho_l=\rho_\infty\left(\frac{p+B}{p_\infty+B}\right)^{1/n_T}, \quad (12)$$

where $n_T=7.15$ and $B=3.046\times10^8$ Pa.

The oscillation of the bubble gas is assumed to be adiabatic

$$\rho_g=\rho_{ref}\left(\frac{p}{p_{ref}}\right)^{1/\gamma_h}, \quad (13)$$

where ρ_{ref} and p_{ref} are the reference density and pressure of the bubble gas, and γ_h is the ratio of the specific heats of the gas, which is assumed to be constant over the time of the observation[80].

To avoid the accumulation of numerical error for the mass of the bubble gas, the density of gas is updated using the conservation of mass, following Koch et al.[51]:

$$\rho_g(t)=\frac{\rho_g(0)V(0)}{V(t)}, \quad (14)$$

where $\rho_g(t)$ and $V(t)$ are the gas density and the volume of the bubble at time t, and $\rho_g(0)$ and $V(0)$ are their initial values. Here, the density of the bubble gas is assumed to be uniform in space.

b. Non-reflective boundary condition at the far field. A finite truncated domain is necessary for numerical modeling to represent the infinite liquid domain. To ensure the non-reflection of shockwaves at the external boundary, a large, truncated domain with the dimension being about $100R_{max}$ is necessary[50,53,54], leading to a considerable demand for computational resources. Here, R_{max} is a bubble's maximum radius in an unbounded, incompressible, inviscid liquid. In the following, we formulate the far-field boundary condition using the asymptotic solution to reduce the size of the truncated domain and avoid the unphysical reflection of shockwaves at the external boundary.

Wang and Blake[39,40] developed the weakly compressible theory for non-spherical bubble dynamics based on the compressible potential flow theory, using the method of matched asymptotic expansions. They obtained the asymptotic analytic solution for the flow far away from a bubble oscillating near a rigid flat boundary, in terms of the velocity potential $\varphi(r,t)$

$$\varphi(r,t)=-\frac{1}{2\pi r}\dot{V}(t-r/c), \quad (15)$$

where $V(t)$ is the transient bubble volume at time t, the over dot denotes the derivative in time t, r is the distance from a field point in the far field to the geometrical center of the bubble, and c is the speed of sound in the liquid. The liquid velocity $\mathbf{u}(\mathbf{r},t)$ in the far field is given as follows:

$$\mathbf{u}(\mathbf{r},t)=u(r,t)\mathbf{e}_r=\left(\frac{1}{2\pi r^2}\dot{V}(t-r/c)+\frac{1}{2\pi cr}\ddot{V}(t-r/c)\right)\mathbf{e}_r, \quad (16)$$

where $\mathbf{e}_r$ is the unit vector from the initial bubble centroid to the field point considered.

The far-field asymptotic solution (16) is obtained based on the potential flow theory but stands for the present viscous model, which is justified as follows. The viscous flow velocity $\mathbf{u}(\mathbf{r},t)$ has the following Helmholtz' s decomposition:

$$\mathbf{u}=\nabla\varphi+\nabla\times\mathbf{A}. \quad (17)$$

The first component is irrotational and described by a scaler potential $\varphi(r,t)$. The second part is rotational, accounting for all the vorticity of the flow, and is described by a vector potential $\mathbf{A}$. To make this decomposition unique, it is assumed that $\nabla\cdot\mathbf{A}=0$. The vector potential $\mathbf{A}$ can be expressed in terms of the vorticity $\omega(\mathbf{r},t)$ as follows:

$$\mathbf{A}=\frac{1}{4\pi}\int_\Omega\frac{\omega(\mathbf{r}',t)}{|\mathbf{r}-\mathbf{r}'|}dV'. \quad (18)$$

In this expression, $\mathbf{r}$ is the field point, and $\mathbf{r}'$ is the position of integration element dV' (the source point). The integral domain Ω is the part of the liquid domain, where the vorticity is nonzero, with a length scale of R_{max}.

Klein and Ting[81] analyzed the far-field asymptotic behavior due to vorticity within a finite domain, with the following result

$$\mathbf{A} = O\left(r^{-2}\right), r \to \infty. \tag{19}$$

The velocity contribution stemming from the rotational component is of $O\left(r^{-3}\right)$, and decays faster than the velocity contribution of $O\left(r^{-2}\right)$ originating from the irrotational component. The far-field behavior of the velocity magnitude is thus given by equation (16) to the first two orders of approximation.

The pressure at the far field is obtained from the Bernoulli equation

$$p = p_\infty - \frac{1}{2}\rho_l u^2 + p_d, \tag{20}$$

where $p_d(r,t) = -\rho_l \frac{\partial \varphi}{\partial t} = \frac{\rho_l}{2\pi r}\ddot{V}(t - r/c)$. We have

$$\int_0^t p_d(r,t)\,dt = \frac{\rho_l}{2\pi r}\int_0^t \ddot{V}(t-r/c)\,dt = \frac{\rho_l}{2\pi r}\left(\dot{V}(t-r/c) - \dot{V}(0-r/c)\right) = \frac{\rho_l}{2\pi r}\dot{V}(t-r/c). \tag{21}$$

Here we used $\dot{V}(-r/c) = 0$, as the bubble oscillation has not started at time $t = -r/c$.

Substituting equations (20) and (21) into equation (16) yields

$$c\rho_l u(r,t) = \frac{c}{r}\int_0^t p_d(r,t)\,dt + p_d(r,t). \tag{22}$$

This equation is similar to the early-time approximations obtained for the fluid-structure interaction by Felippa[82].

Initially, the bubble is spherical, and the flow field can be approximated using the method of images

$$\varphi(r,t) = -\frac{1}{4\pi r}\dot{V}(t-r/c) - \frac{1}{4\pi r_2}\dot{V}(t-r_2/c), \tag{23}$$

where r_2 is the distance from a point considered to the image of the initial bubble centroid in the flat rigid boundary. The initial velocity field is obtained using $\nabla\varphi$, and the initial pressure field is obtained using the Bernoulli equation (20). The first and second order time derivatives of the bubble volume are obtained from the Keller-Miksis equation for spherical bubbles[83]:

$$\left(1 - \frac{1}{c}\dot{R}\right)R\ddot{R} + \frac{3}{2}\dot{R}^2\left(1 - \frac{1}{3c}\dot{R}\right) = \left(1 + \frac{1}{c}\dot{R}\right)\frac{p_l}{\rho_l} + \frac{R}{\rho_l c}\frac{dp_l}{dt}, \tag{24}$$

in which p_l is the pressure of the liquid at the bubble surface and given as follows

$$p_l = p_{b0}\left(\frac{R_0}{R}\right)^{3\gamma_h} - \frac{2\sigma}{R} - (p_\infty - p_v) - \frac{4\mu_l}{R}\dot{R}, \tag{25}$$

where p_{b0} is the initial pressure of the bubble gas, R_0 is the initial bubble radius, R is the transient bubble radius at time t, $\dot{R}$ and $\ddot{R}$ are the first and second derivatives in time t, respectively.

2. Numerical setup

Consider an initially spherical bubble of high internal pressure inserted into the liquid at a standoff distance D from the boundary. As the computations are axisymmetric, a wedge-shaped domain with an opening angle of 2 degrees is constructed, with one cell wide in the azimuthal direction. The two planes shown in figure 3(a) are set as the wedge type in OpenFOAM to ensure axial symmetry. The essentially two-dimensional computational domain is bounded by the axis of symmetry, the flat rigid non-slip wall, and the non-reflective boundary at a distance of R_{dmn} to the origin in all directions.

The cross-sectional view of the mesh is shown in figure 3(b). The grid spacing is uniform in a rectangular domain within the initial bubble. Outside this rectangle, the domain is split into several blocks with the grid spacing growth rate being 1.01. The mesh near the rigid wall is refined to capture the flow within the viscous boundary layer. The adaptive time step is chosen to satisfy the CFL condition[84] with the maximum Courant number being 0.02 when capturing the shock-waves.

3. Numerical validation

a. Validation of the non-reflective boundary condition at far field. Firstly, we validate the effectiveness of the non-reflective boundary condition at the far field. The case considered is a bubble with the maximum radius R_{max} = 600 μm at the dimensionless standoff distance $\gamma = D/R_{max}$ = 1.1. The initial conditions are R_0 = 300 μm, $\dot{R}_0$ = 20 m/s and p_{b0} = 1500 Pa, which are obtained by integrating the Keller-Miksis equations backwards from its maximum radius and zero bubble wall velocity using the fourth-order Runge-Kutta method. Additional details can be found in Wang[85] for reference. The caption to figure 4 provides other parameters used for calculations. This case is calculated with the computational domains being R_{dmn} = 10R_{max} and 100R_{max}, respectively. Figure 4 dis-

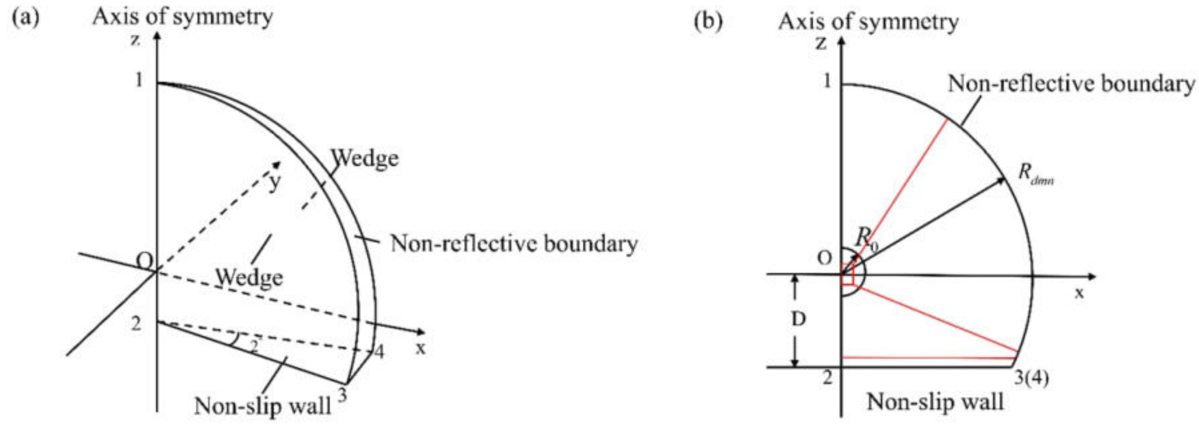

FIG. 3. Sketch of the geometry and the boundary conditions used for the simulations of bubble dynamics near a rigid boundary. (a) 3D view of the truncated computational domain and (b) 2D projection of the computational domain in the Oxz-plane. An initially spherical bubble of high internal pressure is inserted into the liquid at a distance D from the boundary.

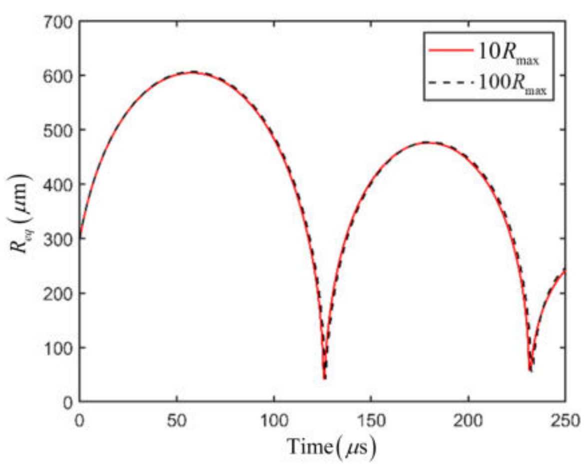

FIG. 4. Comparison of the equivalent bubble radius histories R_{eq} obtained from different computational domain sizes $10R_{max}$ and $100R_{max}$ respectively, for a bubble with the maximum radius R_{max} = 600 μm at the dimensionless standoff distance γ = 1.1 from a rigid boundary. The initial conditions for the computation are R_0 = 300 μm, $\dot{R}_0$ = 20 m/s and p_{b0} = 1500 Pa. Other parameters used for calculations are $\rho_\infty = 998$ kg/m^3, $\rho_{ref} = 1.2$ kg/m^3, $p_\infty = p_{ref} = 101315$ Pa, $\mu_g = 1.73 \times 10^{-5}$ Pa $\cdot$ s, $\mu_l = 0.001$ Pa $\cdot$ s, $\gamma_h = 1.4$, σ = 0 N/m, and c = 1500 m/s.

plays the excellent agreement for the equivalent bubble radius history $R_{eq} = (3V/4\pi)^{1/3}$, although one domain size is ten times larger than the other one. The CPU time is about 50 hours and 71 hours for $R_{dmn} = 10R_{max}$ and $100R_{max}$ respectively, with the Courant number being 0.5. This confirms the accuracy and effectiveness of the non-reflective boundary condition at the far field. Consequently, the domain size is set to $R_{dmn} = 10R_{max}$ for the remaining computations.

b. Convergence tests. The convergence tests are carried out for various element numbers, with the results displayed in figure 5(a) for the time histories of the equivalent bubble radius R_{eq} and figure 5(b) for the bubble shapes at its maximum volume during the second cycle of oscillation. The figures display the convergence of the numerical model. The results for the two higher resolutions, N = 501671 and 756954, are almost identical for the equivalent bubble radius histories and the bubble shapes. Therefore, N = 501671 is chosen for all the remaining calculations.

III. EXPERIMENTAL RESULTS

A. Spherical bubble oscillation in the silicone oil

We first consider a bubble oscillating in an equivalent unbounded domain in the 1000cSt silicone oil with the density ρ_l, the dynamic viscosity μ_l, and the surface tension coefficient σ being 975 kg/m^3, 0.975 Pa $\cdot$ s, and 0.021 N/m, respectively. Figure 6 shows the evolution of bubble shapes for two oscillation cycles. The bubble retains a nearly spherical shape during the oscillations. Figure 7 compares the equivalent bubble radius R_{eq} with the solution of the Keller-Miksis equation (24), where p_{b0} = 659 Pa, R_0 = 14.74 mm, p_∞ = 101315 Pa, γ_h = 1.4. Since the precise sound speed in silicone oils cannot be obtained using our experimental devices, we adapt the sound speed c in the Keller-Miksis equations to 950 m/s to align with the experimental data while ensuring it remains within a reasonable range[86]. As the temperature of the gas is high as a result of the thermal decomposition within the bubble induced by the copper wire, the vapor pressure p_v is set as 31000 Pa in the Keller-Miksis equation to fit with the oscillation period in the experiment. The saturation vapor pressure p_v = 31000 Pa is also employed for determining the initial conditions and updating the far field boundary values in the simulations of bubbles within silicone oils. The theoretical curve in figure 7 for the initial expansion stage is obtained by integrating the Keller-Miksis equations backwards from its maximum radius $R_{max} = R_0$ = 14.74 mm and zero bubble wall velocity $\dot{R}_0 = 0$ m/s with p_{b0} = 659 Pa. There is good agree-

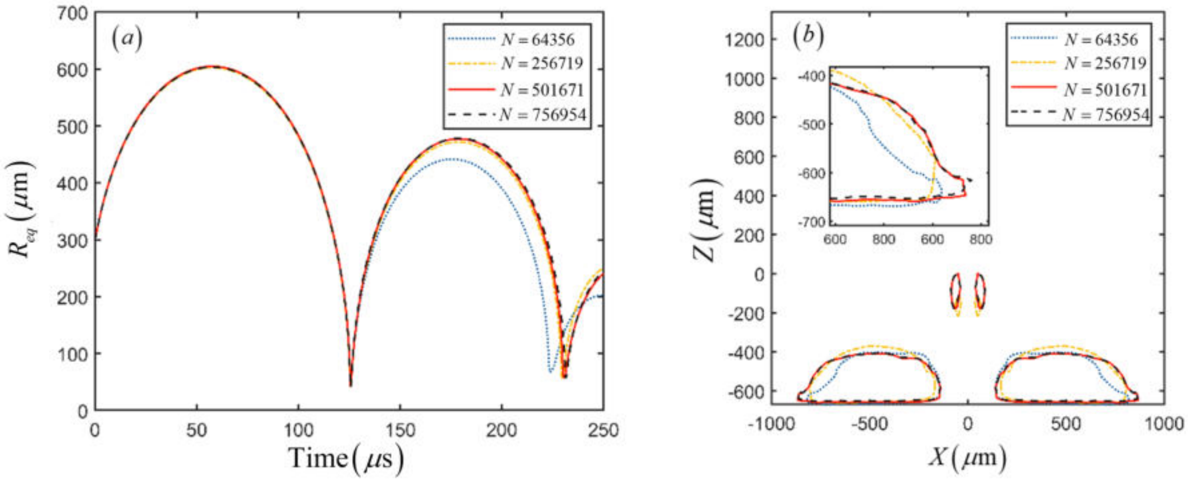

FIG. 5. Convergence tests in terms of various element numbers: 64356, 256719, 501671, and 756954, for (a) the equivalent bubble radius R_{eq} histories and (b) the bubble shapes. Parameters used for calculations are the same as in figure 4.

ment between the experimental results and the Keller-Miksis equation. This agreement justifies the accuracy of the experimental measurements and the Newtonian fluid model with the parameters used in the calculation.

B. Bubble oscillation near a rigid boundary in silicone oils

The dynamics of bubbles near a rigid boundary are now under investigation within three distinct media: water, 500cSt silicone oil, and 1000cSt silicone oil. Properties of the three liquids are listed in table I. The dynamic viscosities of 500cSt and 1000cSt silicone oils are 0.485 Pa · s and 0.975 Pa · s, being much larger than the water viscosity 0.001 Pa · s.

Figure 8 displays the dynamics of a bubble near a rigid flat boundary located at the bottom of each frame for $\gamma \approx 1.4$ in (a) water, (b) 500cSt silicone oil, and (c) 1000cSt silicone oil, respectively. As depicted in figure 8(a), the bubble in water initially undergoes spherical expansion in frames (a1)-(a3). Subsequently, it collapses into a vertically elongated prolate spheroid in frames (a3)-(a7). The bubble then collapses predominantly from the upper surface in frames (a7)-(a9). A jet forms and penetrates the bubble during the early stages of the rebound in frame (a9). As the bubble rebounds, the jet penetrates the liquid between the bubble and the wall, eventually impacting the wall in frames (a9)-(a12). It subsequently re-collapses and migrates to the wall in frames (a12)-(a18) when the instability develops at the bubble surface. The bubble disintegrates towards the end of the second cycle.

Figures 8(b) and 8(c) display similar features for the bubble dynamics in silicone oils. As in the case of water, the bubble expands spherically, first collapsing to a prolate spheroid, which is elongated vertically and then collapsing predominantly from the upper surface. Figure 9 shows the equivalent bubble radii R_{eq} history in the experiment. With much larger viscosities, the bubble maximum radii are smaller in silicone oils, 15.33 mm and 14.03 mm in 500cSt and 1000cSt silicone oils, compared to 16.35 mm in water. This is because of the more significant damping effects in silicone oils. Accordingly, the periods of the first cycle are smaller in silicone oils, being 3.80 and 3.54 ms in 500cSt and 1000cSt silicone oils, compared to 4.18 ms in water.

As in the case of water, a jet forms during the early rebounding of the bubble, penetrating the bubble and then impacting the wall. However, both the maximum bubble radius and the oscillation period in the second cycle are significantly smaller for the bubble in water as in figure 9. This phenomenon is attributed to the additional energy dissipation stemming from surface instability and the formation of bubble clouds following jet impact and penetration through the bubble in water[87–89]. The bubble then re-collapses and migrates to the wall due to the Bjerknes force of the rigid boundary. In contrast to the scenario in water, the bubble maintains stability during the second cycle in the case of silicone oils. As a result, the jet is visible in frames (b11)-(b12) of figure 8(b) and frames (c12)-(c14) of figure 8(c). A protrusion of bubble gas encloses and follows the jet after the jet has penetrated the bubble.

IV. COMPUTATIONAL RESULTS

Computational results are presented and discussed in this section. This includes the validation of the computational model with experiments. Attention is paid to the generation and evolution of vortex sheets, vortex rings, flow fields, shock-wave propagation, jet development and impact on the rigid boundary, and the shear stress at the rigid boundary. These details are either unavailable or difficult to obtain from experiments.

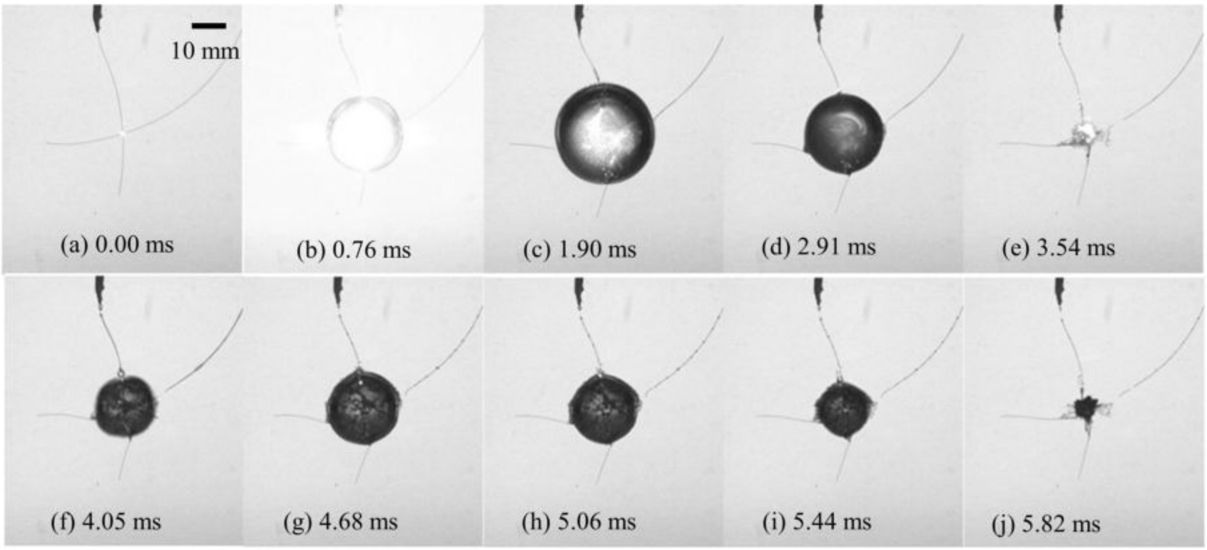

FIG. 6. The evolution of bubble shapes for a spherical bubble oscillating in the 1000cSt silicone oil with the density ρ_l, the dynamic viscosity μ_l, and the surface tension coefficient σ being 975 $\mathrm{kg/m^3}$, 0.975 $\mathrm{Pa\cdot s}$, and 0.021 N/m, respectively.

TABLE I. Properties of the liquids used in the experiment, the Reynolds and Weber numbers, the corresponding maximum equivalent bubble radius R_{max}, and the period for the first oscillation cycle P_1.

Type of Liquid	$\rho_l(\mathrm{kg/m^3})$	$\mu_l(\mathrm{Pa\cdot s})$	σ (N/m)	Re	We	R_{max} (mm)	P_1 (ms)
Water	998	0.001	0.072	1.63×10^5	2.25×10^4	16.35	4.18
500cSt Silicone Oil	975	0.485	0.021	3.08×10^2	7.23×10^4	15.33	3.80
1000cSt Silicone Oil	975	0.975	0.021	1.41×10^2	6.62×10^4	14.03	3.54

A. Comparisons with experiments

We first compare the numerical results with our experimental results for the bubble oscillating in the 500cSt silicone oil with the viscosity being 0.485 $\mathrm{Pa\cdot s}$ and Reynolds number being 3.08×10^2 at the dimensionless standoff distance $\gamma\approx2.0$. The computational domain size is $10R_{max}$ and inital conditions used for calculation are R_0 = 10 mm, $\dot{R}_0 = 12$ m/s and p_{b0} = 720 Pa. Other parameters used for calculations are provided in the caption to figure 10. The computational results are re-timed for the comparisons.

Figure 10 displays the bubble shapes at representative times. The computational and experimental results are shown on the left and right parts of frames (a1)-(f1), respectively. The rigid boundary is at the bottom of frames (a1)-(f1). Frames (a2)-(f2) represent 2D views of the simulated bubbles, while frames (a3)-(f3) present their 3D perspectives. Figure 10(a) is for the bubble at its maximum radius when it remains spherical. It then begins to collapse and becomes a prolate spheroid in figures 10(b)-(c), and a liquid jet forms at the top of the bubble surface, piercing the lower bubble surface in figure 10(d). A toroidal bubble accompanied by a protrusion of the lower bubble surface forms and expands towards the rigid boundary during the rebound in figure 10(e) and then reaches its second maximum volume in figure 10(f). The computation agrees well with the experiment for a bubble collapsing and rebounding in the 500cSt silicone oil at a moderately large Reynolds number.

We then compare the computational results with the experiment[57] where the Reynolds number is Re = 6033. Parameters used for calculations are the same as in figure 4. The computational results are also re-timed for the comparisons. Figure 11 displays the bubble shapes at representative times. The computational and experimental results are shown on the left and right parts of frames (a1)-(f1), respectively. The rigid boundary is at the bottom of frames (a1)-(f1). Frames (a2)-(f2) represent 2D views of the simulated bubbles, while frames (a3)-(f3) present their 3D perspectives. Figure 11(a) is for the bubble at its maximum radius when it remains spherical apart from its surface near the wall being flattened by the wall. During the late collapse stages, a liquid jet forms at the top of the bubble surface in figure 11(b) and impacts at the opposite bubble surface in figure 11(c). After the jet penetrates the bubble wall, a toroidal bubble forms, collapses continuously to its minimum volume, and rebounds in figure 11(d). It then reaches its second maximum volume in figure 11(e) and later re-collapses in figure 11(f).

The computation repeats all these features observed in the experiment for the bubble expansion, collapse, rebound, and re-collapse. The computational results for the bubble shapes agree with those of the experiment during the first and second oscillation cycles. The jet is not observable in the experiments

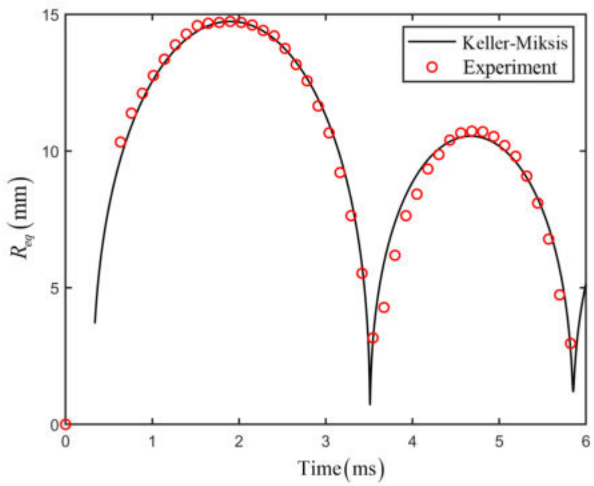

FIG. 7. Comparison of the equivalent bubble radius R_{eq} history with the solution of the Keller-Miksis equation for a spherical bubble oscillating in the 1000cSt silicone oil for the case in figure 6. Other parameters used for the Keller-Miksis equation are p_{b0} = 659 Pa, R_0 = 14.74 mm, p_v = 31000 Pa, p_∞ = 101315 Pa, γ_h = 1.4, and c = 950 m/s.

because of the reflection of light off the liquid/gas interface; nevertheless, the outer profile of the toroidal bubble of the computation has excellent agreement with that of the experiment.

Figure 12 compares the equivalent bubble radius R_{eq} history between the computation and the experiment[57]. The excellent agreement is shown for the first and second cycles of oscillation. The relative error of the maximum radius in the second cycle is about 7%, which may be due to the heat transfer and the phase change neglected in the model and/or the measurement errors in the experiment.

It is challenging to compute the energy loss of a bubble system associated with the emission of shockwaves at the end of the collapse. Typically, this has been handled by empirically removing a part of the bubble potential energy at the end of the first cycle of oscillation[57]. Otherwise, subsequent numerical results are incorrect. Without resetting the rebounding condition, our computational results agree well with the experiments for the second cycle of oscillation.

B. Bubble dynamics near a rigid boundary for $Re = O(10)$

In this subsection, we conduct numerical simulations of bubble dynamics near a rigid boundary for a Reynolds number of $O(10)$ and study the viscous effects on bubble dynamics near a rigid boundary. We will re-compute the case in figure 11 for Re = 6033 by setting Re = 75 (with μ_l = 0.08 Pa $\cdot$ s), with all other parameters kept unchanged.

1. Vortex ring development

Figure 13 displays the streamlines and velocity vectors outside and inside the bubble and the velocity and pressure contours inside the bubble. When the bubble is nearly spherical, a stagnation point exists at the center of the bubble, from which the streamlines radiate outwards, as shown in figure 13(a). The part of the bubble surface furthest from the wall expands faster than the closer part, as the latter is hindered by the wall. Consequently, the airflow above the stagnation point moves faster than the airflow below the stagnation point, and the airflow above the stagnation point has smaller pressure, as shown in figure 13(b). This is consistent with the Bernoulli equation.

As a result of the pressure gradient, the stagnation point moves away from the wall along the axis of symmetry during expansion. Two kinds of streamlines form: concave shape for the upper part and convex shape for the lower part, as shown in figure 14(a). The streamlines are becoming denser closer to the upwards-moving stagnation point. The concave- and convex- streamlines tend to converge at the stagnation point with different velocities, and the strong velocity difference leads to the formation of the vortex sheet near the upper bubble surface as shown in figure 14(b).

The vortex sheet subsequently approaches the bubble interface and begins transferring momentum to the gas-liquid interface, which in turn influences the flow in the liquid close to the bubble wall. At approximately the moment the bubble achieves maximum volume, the stagnation point meets the bubble surface in figure 15(a) and moves out of the bubble afterward in figure 15(b). The part of the vortex sheet within the bubble decays after it meets with the interface, where it is subject to the much higher shear stress from the liquid with a much higher viscosity than gases. Due to the higher pressure zone at the stagnation point, the liquid flow above it is stopped, the part of the bubble surface furthest from the wall collapses first, and the receding bubble surface drags the surrounding liquid towards it, as observed by Lechner et al.[53]. In the meantime, the part of the bubble surface nearest to the wall still expands, pushing the liquid between the bubble and rigid boundary outward. This generates a circulation around the periphery of the cross-section of the bubble. A vortex ring is accordingly generated within the bubble gas at the outer rim of the vortex sheet.

During the collapse phase, the distal part of the bubble surface from the wall collapses faster, the surrounding liquid flow towards the distal part strengthens, and the vortex ring intensifies, as shown in figures 16(a) and 16(b). These three events enhance each other during collapse, forming a positive feedback loop. A high-speed liquid jet develops, and it gets accelerated by the vortex ring at the bubble surface, which subsequently penetrates the bubble, from which it is redirected outwards after impacting on the wall as shown in figures 16(c) and 16(d). This strengthens the circulation around the vortex ring even further.

With the core of the vortex ring inside the bubble gas, much less energy loss occurs than inside the liquid. This is because the energy dissipation of a vortex ring is proportional

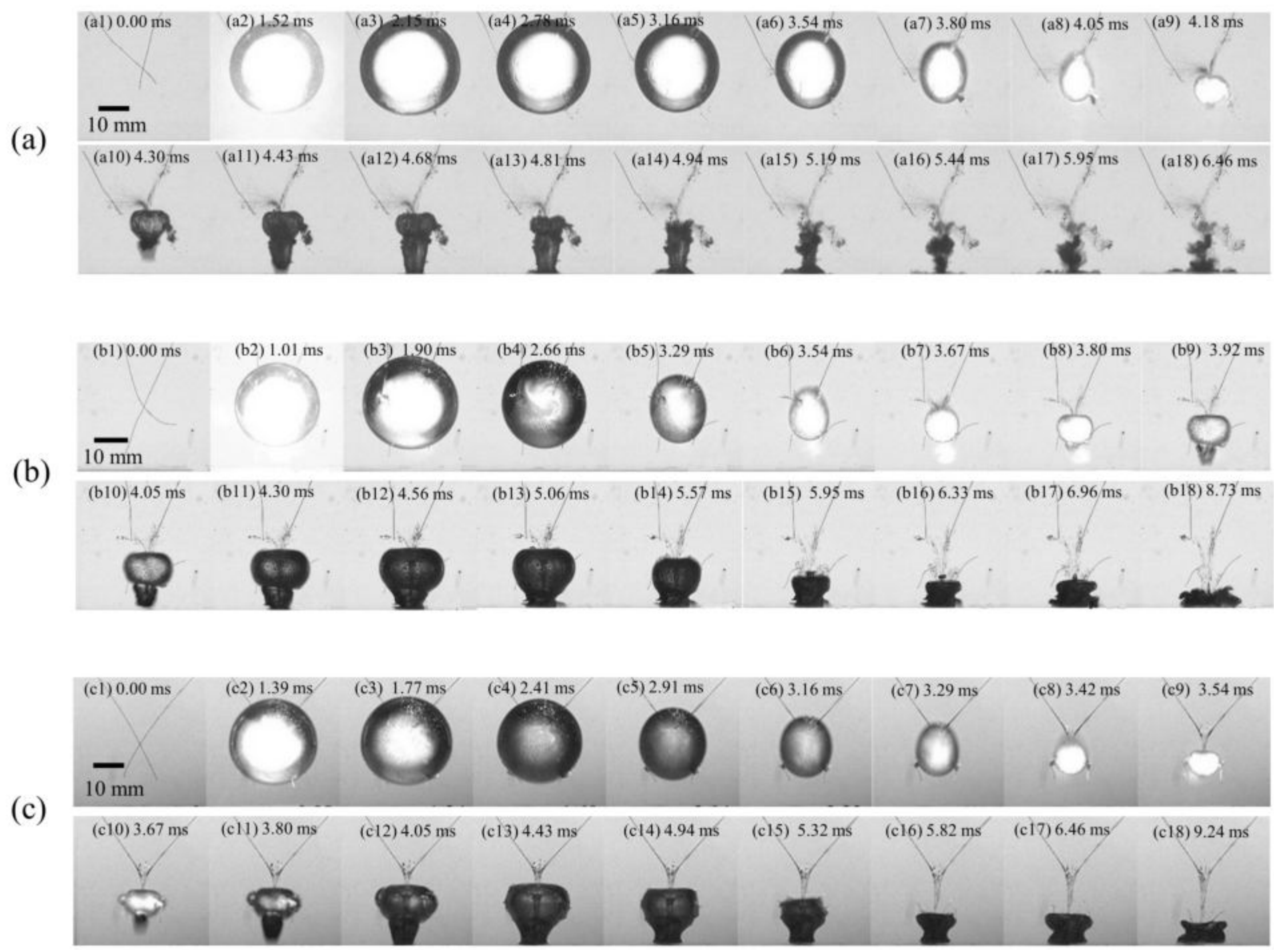

FIG. 8. The evolution of bubble shapes for a bubble oscillating near a rigid boundary in (a) water with the viscosity μ_l being 0.001 $\mathrm{Pa\cdot s}$, (b) 500cSt silicone oil with the viscosity μ_l being 0.485 $\mathrm{Pa\cdot s}$, and (c) 1000cSt silicone oil with the viscosity μ_l being 0.975 $\mathrm{Pa\cdot s}$ at the dimensionless standoff distance $\gamma \approx 1.4$. The densities ρ_l are 998, 975, and 975 $\mathrm{kg/m^3}$, respectively. The surface tension coefficients σ are 0.072, 0.021, and 0.021 N/m, respectively. The maximum bubble radii R_{max} attained in the experiment are about 16.35, 15.33, and 14.03 mm, respectively.

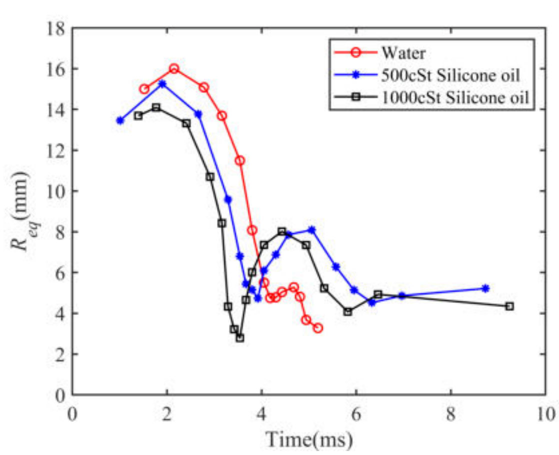

FIG. 9. The equivalent bubble radii R_{eq} history in the experiment for cases in figure 8.

to viscosity, and most of the energy dissipation occurs near its center[90]. With its core inside the bubble gas, the vortex ring accelerates the jet like a bearing system.

The vortex ring associated with a toroidal bubble has been an essential topic for bubble dynamics and plays a key role in toroidal bubble dynamics[36,91–95]. With the concept of ideal fluid mechanics, the generation of the vortex ring is attributed to the topological transform of the liquid domain after the bubble jet penetrates through the bubble. Here, we have revealed that the generation process of the vortex ring takes place within the bubble gas before the bubble jet penetrates through the bubble.

The results on the vortex sheet and the vortex ring provide two mechanisms for the nanodroplet injection model[60,61]. Both the decay of the vortex sheet as it interacts with the bubble interface and the vortex ring adjacent to the bubble interface are potential sources of nanodroplets in the hot bubble gas.

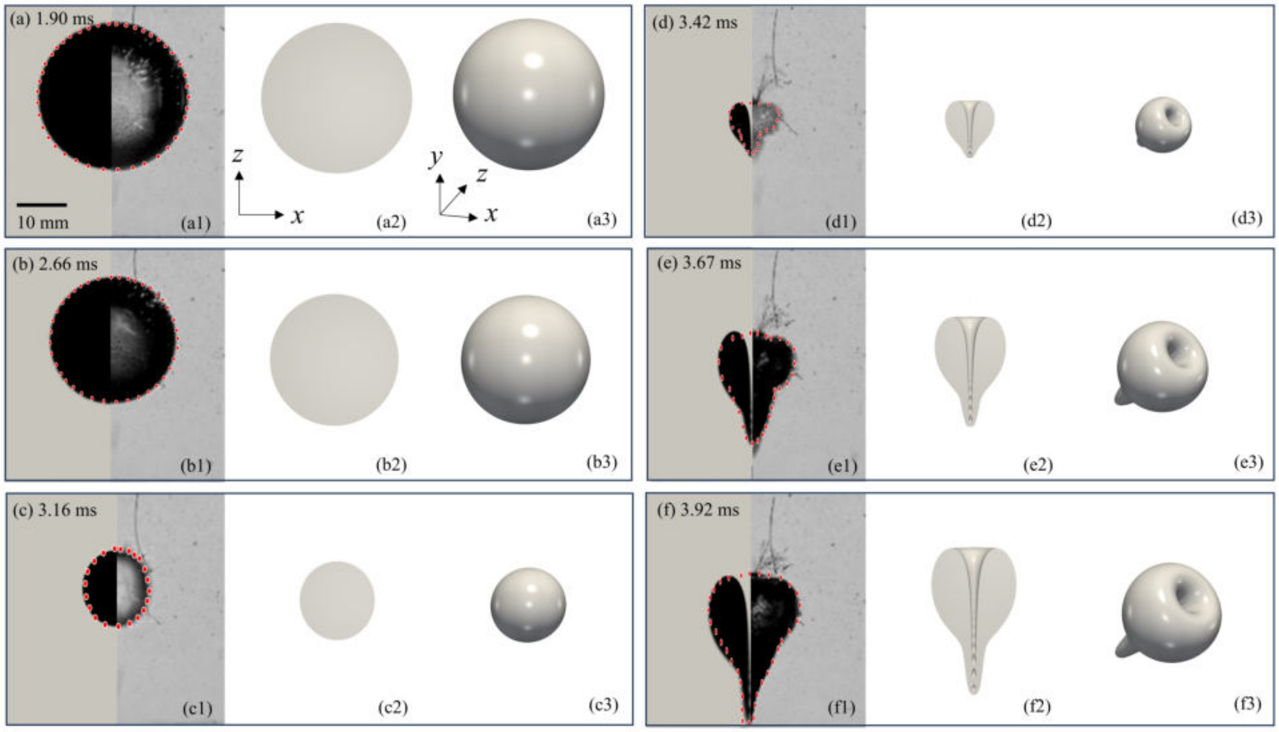

FIG. 10. Comparison of bubble shapes between the computation and the experiment for the bubble oscillating in the 500cSt silicone oil with the viscosity being 0.485 Pa $\cdot$ s at typical times (a) 1.90 ms, (b) 2.66 ms, (c) 3.16 ms, (d) 3.42 ms, (e) 3.67 ms, and (f) 3.92 ms. Parameters used for the calculation are R_0 = 10 mm, $\dot{R}_0 = 12$ m/s and p_{b0} = 720 Pa, $\rho_\infty = 975$ kg/m^3, $\mu_l = 0.485$ Pa $\cdot$ s and c = 950 m/s, and the remaining parameters are the same as in figure 4. The left part in frames (a1)-(f1) is the computational results, while the right is the experimental results. The rigid boundary is the lower boundary of frames (a1)-(f1). The red dot displays the outer profile of the bubble shapes in the experiment. Frames (a2)-(f2) and frames (a3)-(f3) are 2D and 3D views of the simulated bubbles, respectively.

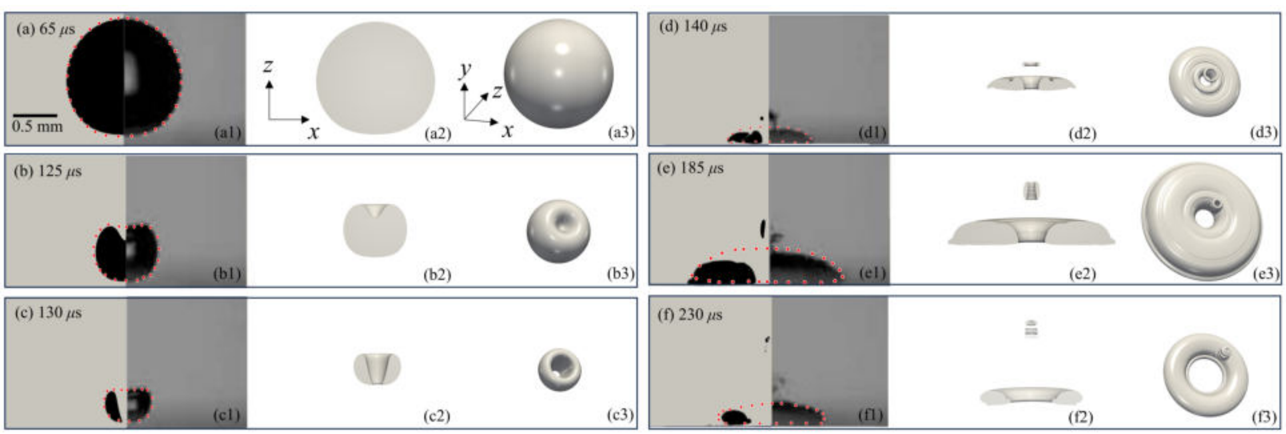

FIG. 11. Comparison of the bubble shapes between the computation and the experiment[57] at typical times (a) 65 μs, (b) 125 μs, (c) 130 μs, (d) 140 μs, (e) 185 μs, and (f) 230 μs during the two cycles of oscillation. The parameters used for calculation are the same as in figure 4. The left part in frames (a1)-(f1) is the computational results, while the right is the experimental results. The rigid boundary is the lower boundary of frames (a1)-(f1). The red dot displays the outer profile of the bubble shapes in the experiment. Frames (a2)-(f2) and frames (a3)-(f3) are 2D and 3D views of the simulated bubbles, respectively.

2. Bubble oscillation and jetting

As shown in figure 17, the bubble expands without significant change to the maximum volume from figure 17(a) to 17(b) for the two Reynolds numbers. At the larger Reynolds number, the jet forms earlier in figure 17(c) and develops to a larger and sharper jet in figure 17(d). When the jet impacts the opposite bubble surface in figure 17(d), the jet at the larger Reynolds number is nearer to the rigid boundary. Similar vis-

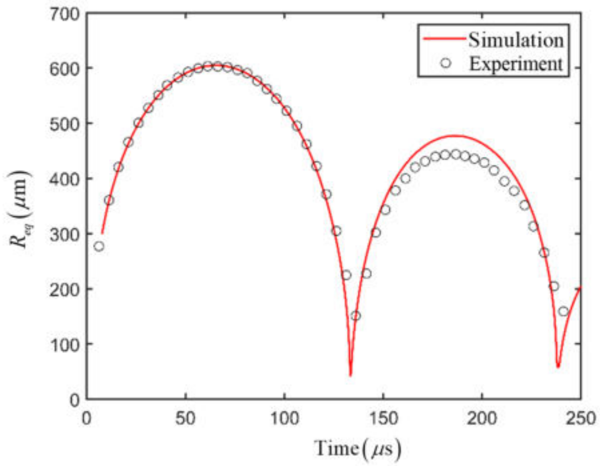

FIG. 12. Comparison of the equivalent bubble radius R_{eq} history between the computation and the experiment[57] for the case of Re = 6033 in figure 11. The parameters used for the calculation are the same as in figure 4.

cous effects on bubble shapes were observed by Minsier et al.[49]. The bubble for Re = 6033 rebounds to a larger maximum volume as shown in figure 17(e).

In figure 18(a), the equivalent bubble radius R_{eq} histories are compared for the two Reynolds numbers: $Re = 75$ and Re = 6033. The first cycle experiences a marginal reduction in both the maximum bubble radius and period at $Re = 75$, attributed to viscous dissipation. For $Re = 75$, a smaller jet is formed in figure 17(d), leading to an increase in the kinetic energy associated with the collapse process. Following the more intense collapse, a greater amount of energy is dissipated through the emission of shockwaves towards the end of the collapse. Consequently, the bubble rebounds to a much smaller maximum radius and period during the second cycle at $Re = 75$.

Figure 18(b) shows the jet velocity V_{jet} histories with the time counted from the jet starting (t = 114 μs for Re = 6033 and t = 116 μs for $Re = 75$) in figure 17(c) to the jet impacting on the opposite bubble wall (t = 122 μs for Re = 6033 and t = 123 μs for Re = 75) in figure 17(d). For Re = 6033, the jet velocity firstly increases with time and then reaches a nearly constant value, which was also observed by Minsier et al.[49]. However, for Re = 75, the jet velocity increases continuously before impacting at the opposite surface, and it attains a larger value than for Re = 6033.

3. Shockwave emission and pressure on the wall

Shockwaves are emitted at the end of collapse and are associated with significant energy loss of the bubble system[37]. The shockwaves are believed to be the leading cause of the erosion of the rigid boundary[17,96]. The pressure contours in figure 19 display the emission and propagation of shockwaves for Re = 75. A ring shockwave emits from the bubble ring at the end of the collapse in figure 19(a), propagates with a circular cross-section in figure 19(b), and impacts itself at the axis of symmetry resulting in a higher pressure in figure 19(c). As a result of the further propagation of the shockwaves, two intersection points exist on the symmetry axis where the pressure is higher in figure 19(d). The two intersection points move in opposite directions in figure 19(e), and a high-pressure region forms when the shockwaves reach the rigid boundary. Subsequently, a clear reflection moving away from the rigid boundary can be observed in figure 19(f). Similar phenomena were observed by Lechner et al.[53].

Figure 20 shows the pressure on the center point of the rigid boundary (green spots in figure 19) as a function of time for Re = 75, 6033. The stronger collapse at Re = 75 leads to the stronger shockwave emission, and thus, the pressure on the rigid boundary is also larger. However, the shockwaves are much weaker, and the pressure on the rigid boundary is much smaller at the end of the second cycle for $Re = 75$ due to greater energy loss at the end of the first cycle of oscillation.

4. Shear stress on the rigid boundary

Figure 21 shows the spatial-temporal distribution of the shear stress τ on the rigid boundary for $Re = 75$, using $\log_{10}|\tau|$ due to its large range of values. The direction pointing away from the axis of symmetry is defined as positive and plotted in red. The direction pointing to the axis of symmetry is negative and plotted in blue. As the bubble expands, it drives the liquid outwards, and the shear stress at the wall is outwards. Starting from the late stages of expansion for $t \geq 40$ μs, the shear stress turns inwards far away from the axis of symmetry. The transition from outwards to inwards shear stress corresponds to the stagnation ring.

The mechanism of the stagnation ring is explained as follows. Figure 22 shows the flow field distribution at t = 42 μs when the bubble is at the late stages of expansion. At certain late stages of expansion, the bubble gas pressure is lower than the hydrostatic pressure. The liquid around the bubble moves outwards owing to its inertia, and the part of the liquid near the wall has less velocity because of the shear stress of the wall. Therefore, the reversed flow towards the center starts near the wall, far away from the axis of symmetry before the end of the expansion, resulting in the stagnation ring occurring before the end of the expansion.

The stagnation ring exists over the wall, with its radius decreasing as the bubble further expands and then collapses. During the late collapse and before rebound for 95 μs $\leq t \leq$ 120 μs, the shear stress is negative everywhere on the boundary and reaches its maximum absolute value. This is generated by the fast-shrinking bubble.

The above feature is repeated during the second cycle of oscillation. During a large part of the rebounding, the shear stress is outwards everywhere due to the fast-spreading jet along the boundary, and a stagnation ring occurs during the later stages of the rebound, with its radius decreasing with time. However, the shear stress distribution is complex and changes rapidly due to the complex flow field caused by the toroidal bubble collapse at the end of the second cycle. The above phenomena were also observed by Zeng et al.[57].

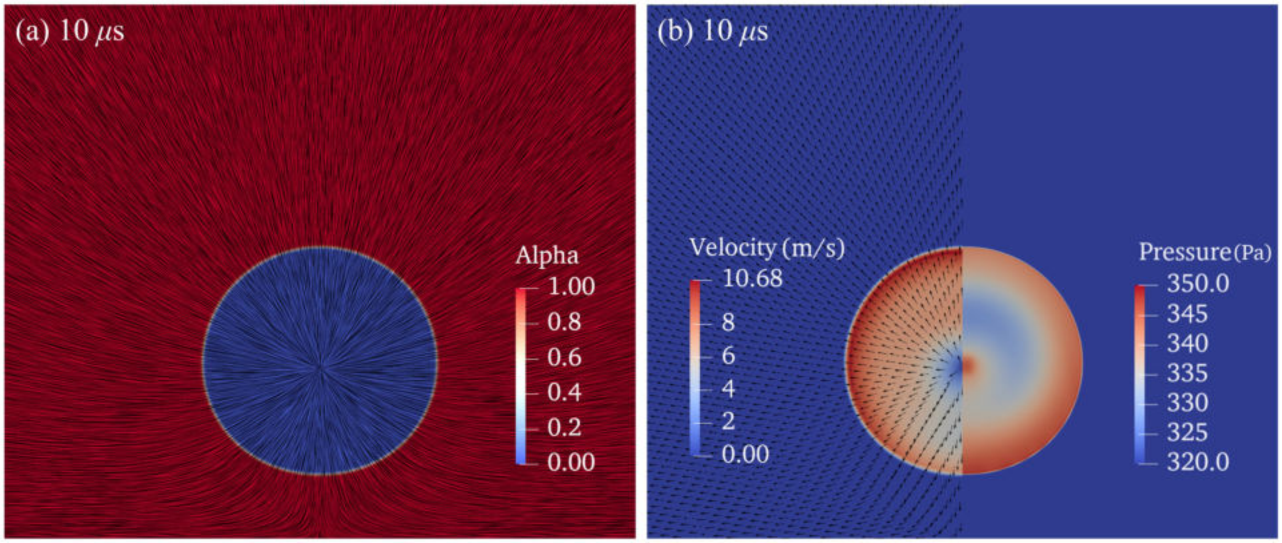

FIG. 13. (a) Streamlines, (b) velocity vectors (left), velocity contour (left), and pressure contour (right) during early expansion when the bubble is nearly spherical. The Reynolds number is $Re = 75$ ($\mu_l = 0.08$ Pa · s), and the remaining parameters are the same as in figure 4.

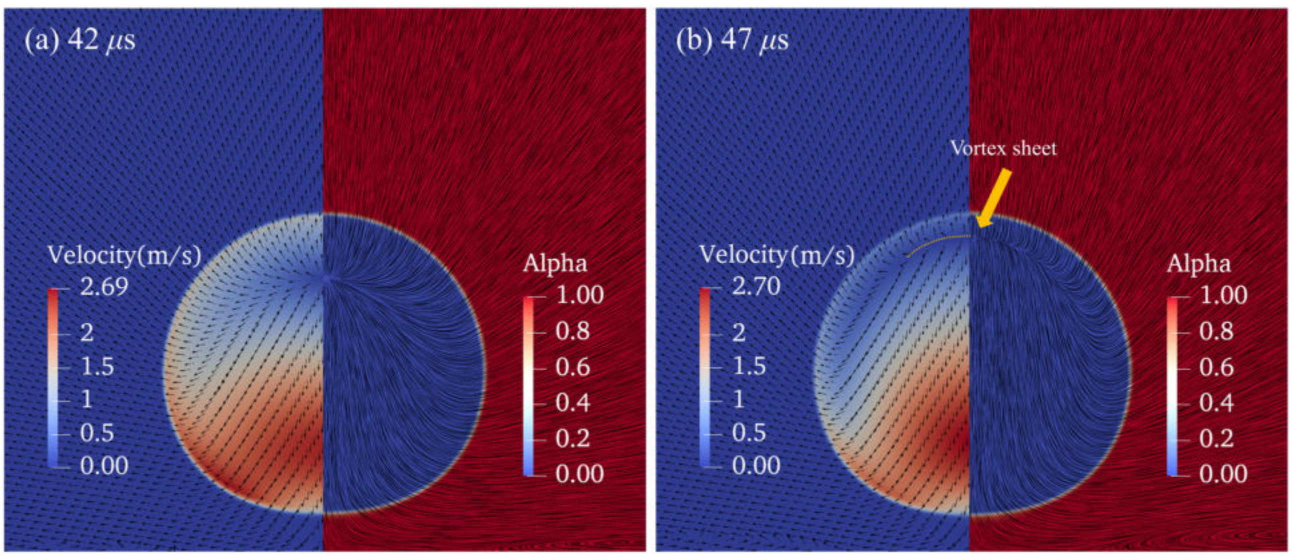

FIG. 14. Velocity vectors (left in each figure), velocity contours (left in each figure), and streamlines (right in each figure) at (a) 42 μs and (b) 47 μs showing the formation of the vortex sheet generated from the bubble collapse near a rigid boundary for the case of $Re = 75$ in figure 13. (Recall that the simulations are axisymmetric when visualizing the 3D form of the vortex sheet).

Figure 23 shows the time histories of the shear stress at a probe point on the rigid boundary 180 μm from the axis of symmetry (green spots in figure 24). For both cases, a distinct impulse with a greater magnitude and a shorter period is evident, along with a more gradual impulse characterized by a smaller magnitude and a longer period. The shear stress for $Re = 75$ is larger than that for $Re = 6033$.

Figure 24 displays the bubble shapes and the flow fields for $Re = 75$ at different times during collapse and rebound, where the probe point is marked as green spots. Figure 24(a) is at $t = 120$ μs when the shear stress is negative and small at the probe point. Figure 24(b) is at $t = 123$ μs when the shockwaves impact the probe point, resulting in the sharp impulse of shear stress in figure 23. Figure 24(c) is at $t = 127$ μs, corresponding to the milder impulse of shear stress in figure 23, when the jet is spreading along the wall after impacting on the rigid boundary. At $t = 150$ μs in figure 24(d), the jet is still spreading, but the magnitude is much smaller, which corresponds to the decreasing wall shear stress in figure 23.

In conclusion, when a bubble undergoes inertial collapse near a rigid boundary, significant shear stress emerges primarily during the propagation of the shockwaves along the boundary and the spread of the jet along the boundary. The former has a much higher amplitude, and the latter has a longer period. They both increase with decreasing Reynolds number.

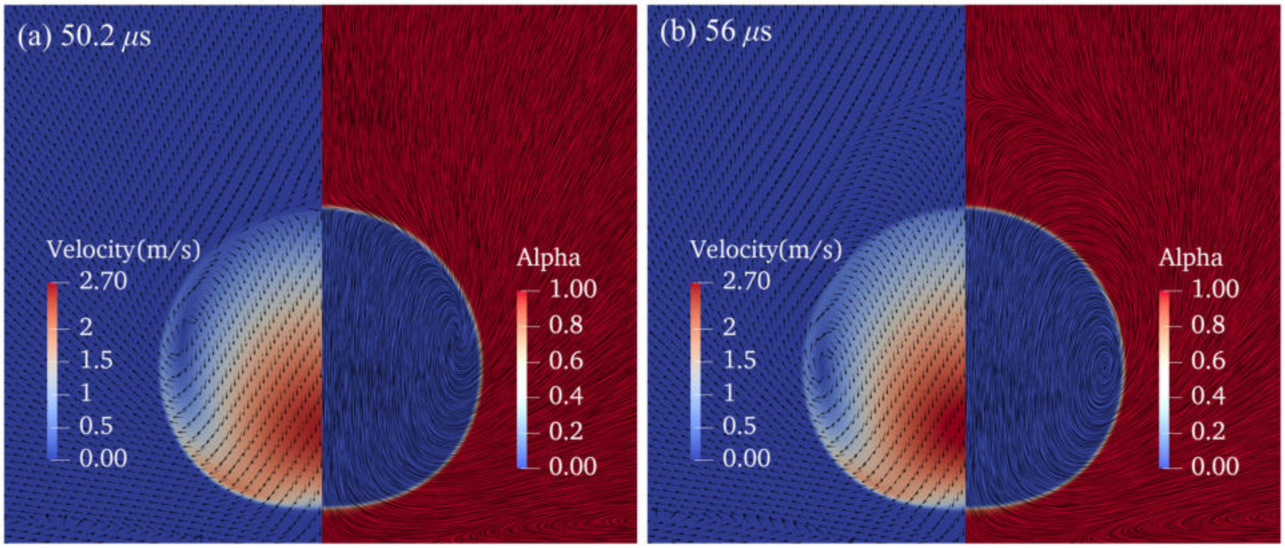

FIG. 15. Velocity vectors (left in each figure), velocity contours (left in each figure), and streamlines (right in each figure) at (a) 50.2 μs and (b) 56 μs showing the conversion from the vortex sheet to the vortex ring for the case of Re = 75 in figure 13.

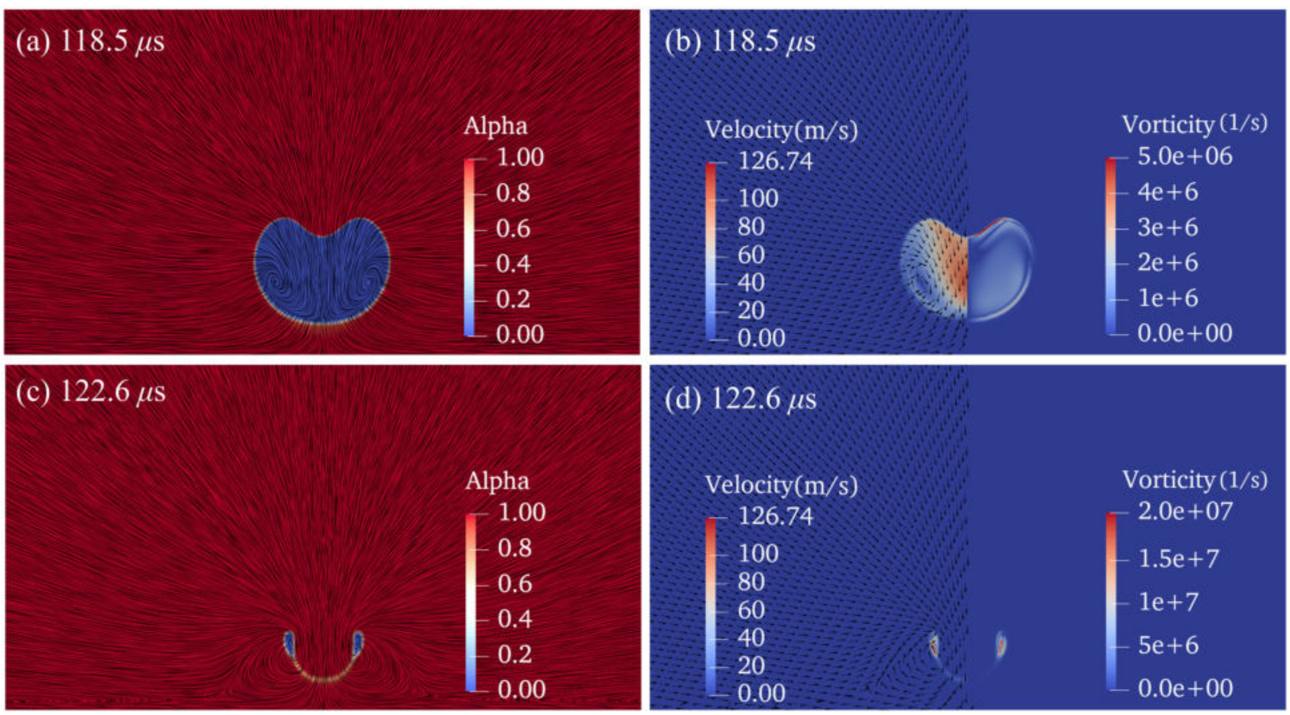

FIG. 16. Streamlines ((a) & (c)), velocity vectors (left in (b) & (d)), velocity contours (left in (b) & (d)), and vorticity contours (right in (b) & (d)) showing the further development of the vortex ring after generation during bubble collapse for the case of Re = 75 in figure 13.

V. SUMMARY AND CONCLUSIONS

Bubble dynamics near a rigid boundary for Reynolds number O(10-100) are studied experimentally using high-speed photography of spark-generated bubble oscillation in silicone oils, whose viscosities are about three orders larger than water. They have also been studied numerically by solving the compressible Navier-Stokes equations by extending the open-source code OpenFOAM. A non-reflective boundary condition at the far field is proposed based on the asymptotic behavior, which allows for a tenfold reduction in the size of the computational domain. New dynamic features are revealed.

a. Mechanisms underlying the bubble jetting and vortex ring. During expansion, the distal part of the bubble surface from the wall expands faster than the closer part, as the latter is hindered by the wall. Accordingly, the bubble gas on the distal

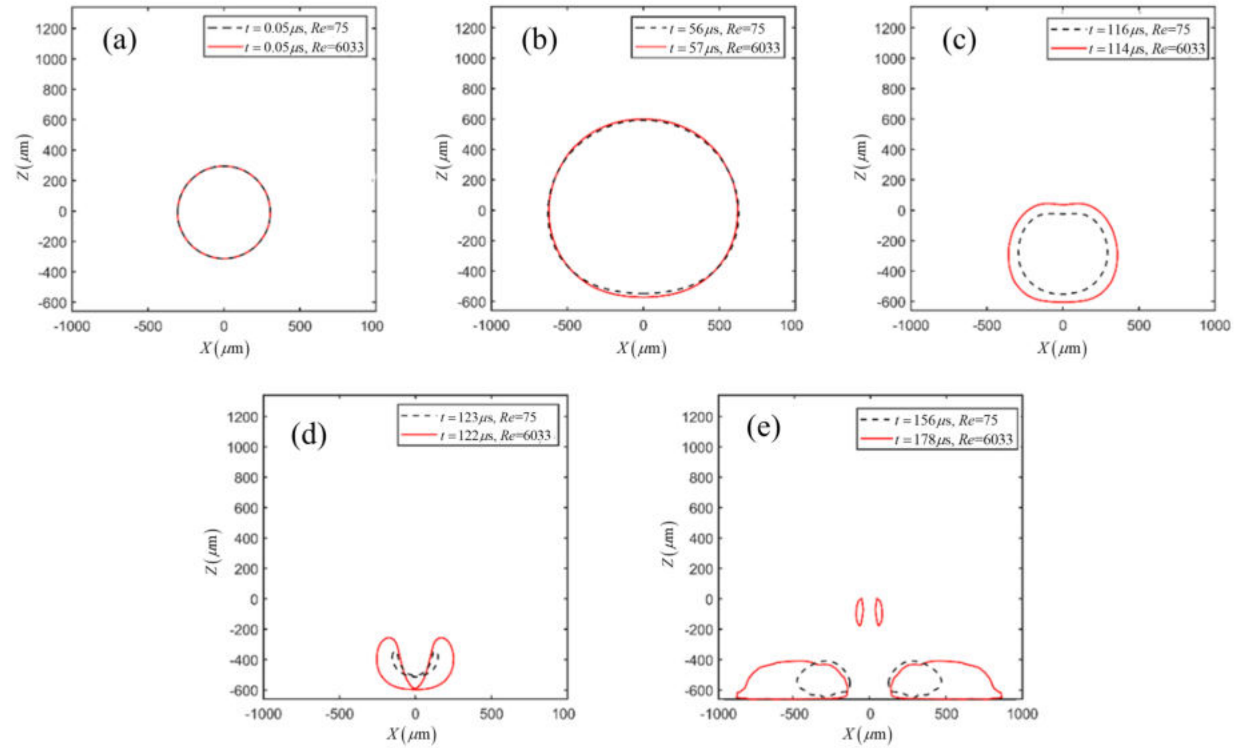

FIG. 17. Bubble shapes evolutions near a rigid boundary for Re = 75, 6033 (μ_l = 0.08, 0.001 Pa · s, respectively). The remaining parameters are the same as in figure 4.

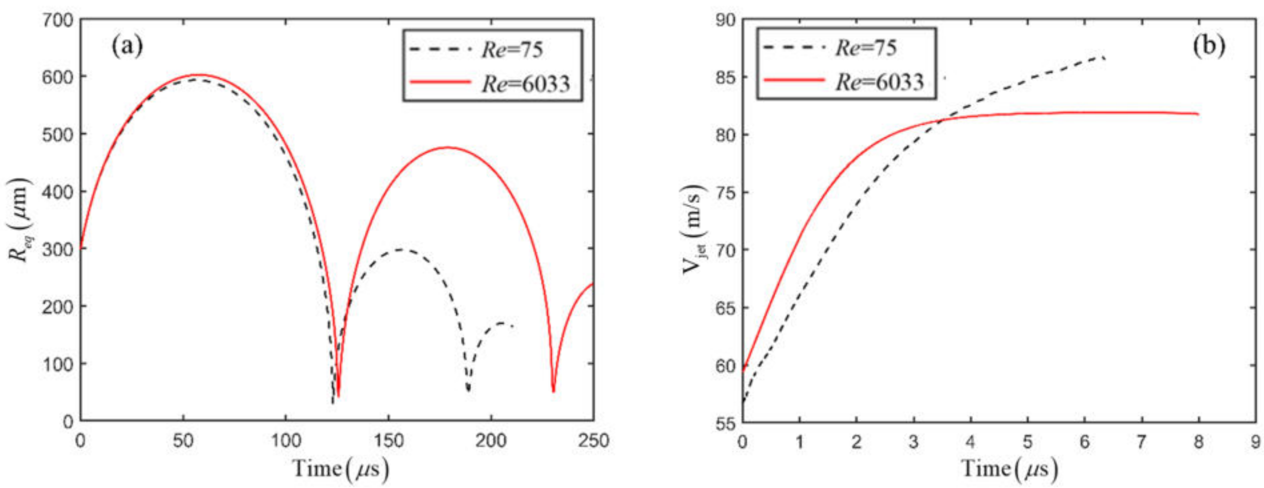

FIG. 18. Numerical results for Re = 75, 6033 (μ_l = 0.08, 0.001 Pa · s, respectively): (a) histories of the equivalent bubble radius R_{eq} and (b) the jet velocity V_{jet} with the time counted from the jet starting (t = 114 μs for Re = 6033 and t = 116 μs for Re = 75). The remaining parameters are the same as in figure 4.

side flows faster away from the stagnation point, initially at the bubble center, and has smaller pressure according to the Bernoulli equation. As a result, the stagnation point moves away from the wall during expansion, and a vortex sheet forms inside the bubble as the streamlines converge to the stagnation point with different velocities.

As the vortex sheet approaches the bubble interface, it transfers momentum to the gas-liquid interface, influencing the liquid flow close to the bubble wall. At approximately the maximum bubble volume, the stagnation point moves out of the bubble. The high-pressure zone at the stagnation point drives the distal bubble surface to collapse first and fastest, pulling the side liquid inwards, as observed by Lechner et al.[53]. In the meantime, the part of the bubble surface nearest

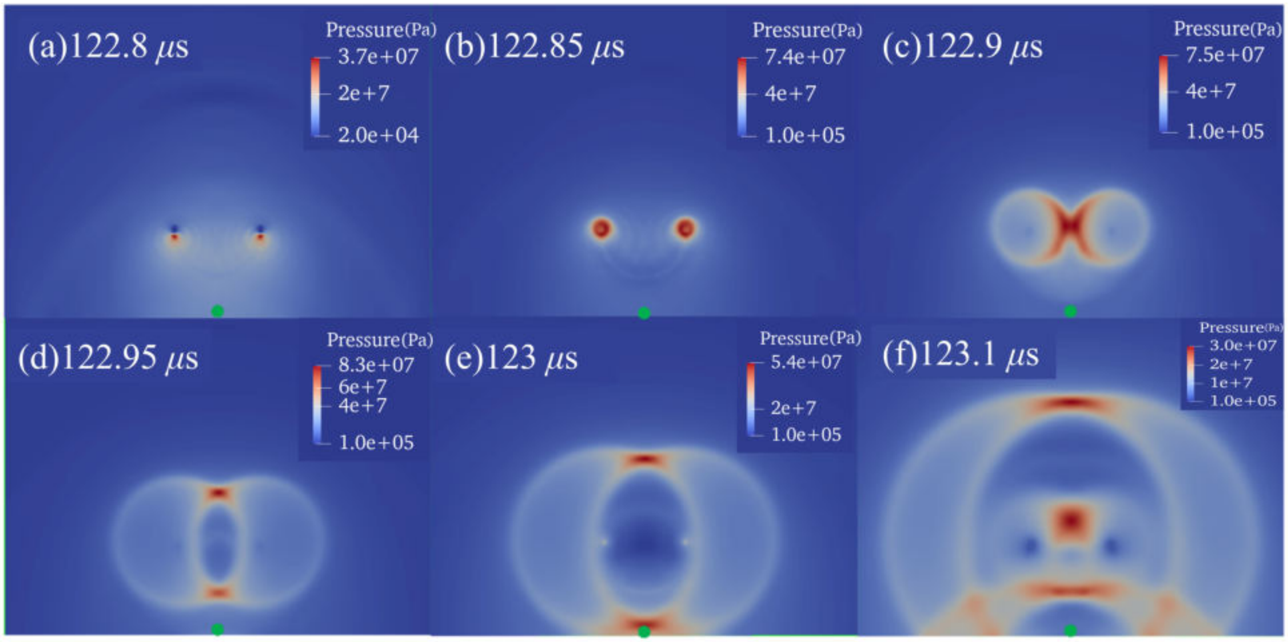

FIG. 19. Pressure contours showing the emission and propagation of shockwaves generated at the end of the first bubble collapse for the case of $Re = 75$ in figure 13.

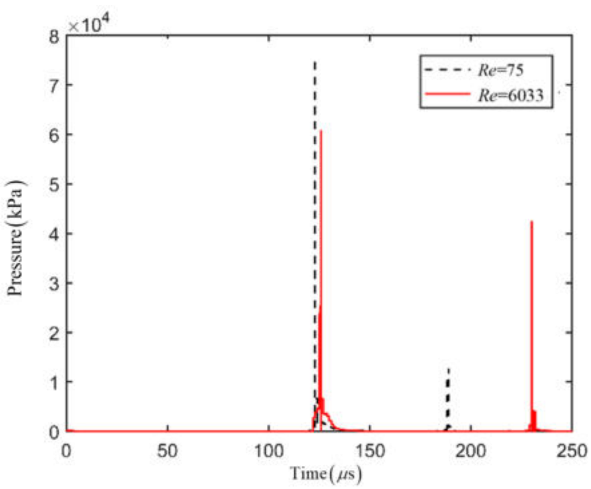

FIG. 20. Pressure on the center point of the rigid boundary (green spots in figure 19) as a function of time for $Re = 75$, 6033 ($\mu_l = 0.08$, 0.001 Pa·s, respectively). The remaining parameters are the same as in figure 4.

the wall still expands, pushing the liquid between the bubble and the rigid boundary outwards. This generates a circulation around the side cross-section of the bubble. A vortex ring is accordingly generated within the bubble gas at the outer rim of the vortex sheet as the vortex sheet decays, owing to the higher shear stress from the liquid.

The distal bubble surface collapses faster during the collapse, the liquid flow towards the distal part strengthens, and the vortex ring intensifies. These events enhance each other in a positive feedback loop. A high-speed liquid jet develops at the distal bubble surface, accelerated by the vortex ring. The liquid jet subsequently penetrates the bubble and is redirected outwards after impacting the wall. This in turn strengthens the circulation around the vortex ring.

With the core of the vortex ring inside the bubble gas, much less energy loss occurs than inside the liquid. This is because the energy dissipation of a vortex ring is proportional to viscosity, and most energy dissipation occurs near its center. With its core inside the bubble gas, the vortex ring accelerates the jet like a bearing system. These new insights into the gas flow inside the bubble provide supporting evidence for the nanodroplet injection model.

b. Viscous effects. The jet is shallower due to viscosity effects and has less kinetic energy at a smaller Reynolds number, as observed by Minsier et al.[49]. With less kinetic energy associated with the jet, the bubble collapses violently to a smaller minimum value, producing stronger shockwaves. With significantly more energy radiated due to the stronger shockwaves, the subsequent oscillation during the second cycle has a smaller maximum radius. The period of oscillation is energy dependent; therefore, the period also reduces due to the energy reduction.

The pressure on the wall is more significant due to the stronger shockwave emission at the end of the first cycle when the Reynolds number is smaller. As more energy is radiated due to stronger shockwaves at the end of the first cycle, the shockwaves are much weaker, and the pressure on the rigid boundary is much smaller at the end of the second cycle.

An oscillating bubble in a higher viscous liquid is more stable. A bubble often breaks up after the first cycle of oscillation in water. A bubble often remains stable in higher viscosity liquid after multiple oscillation cycles.

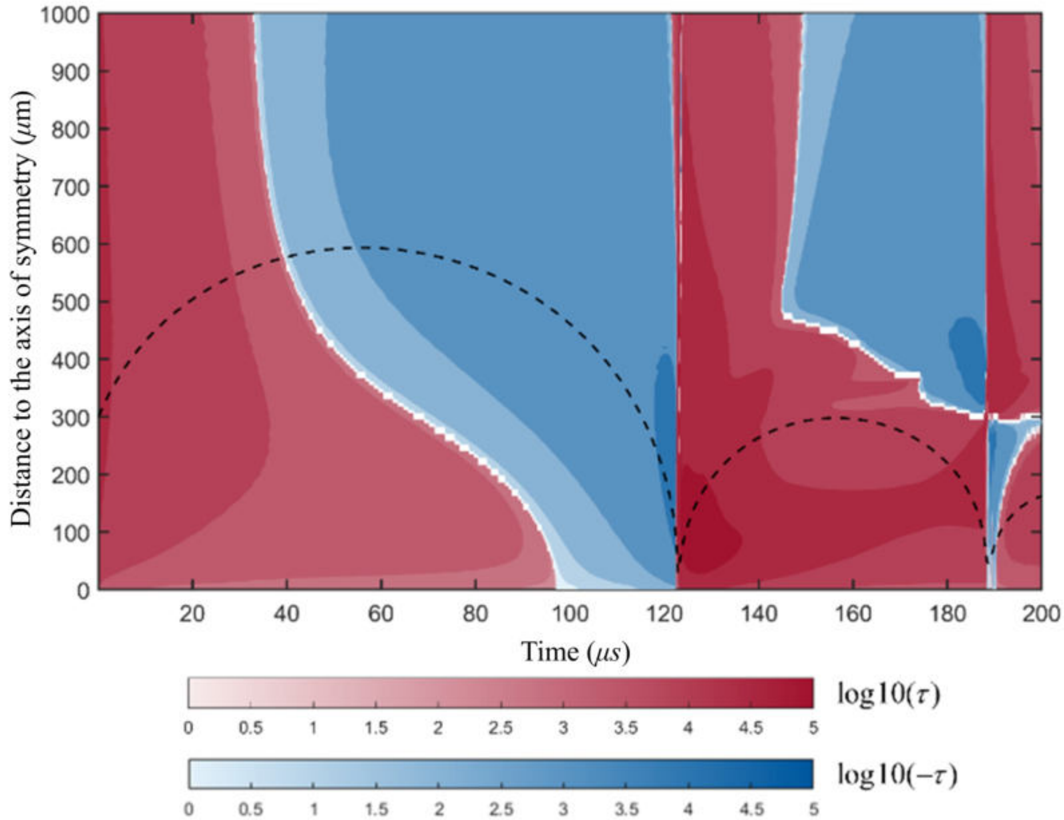

FIG. 21. The time-space map of the wall shear stress for the case of Re = 75 in figure 13. The logarithm to the base 10 is taken of the wall shear stress values before plotting due to the large range of values. The first color bar represents the positive wall shear stress (away from the axis of symmetry), while the second one represents the negative wall shear stress. Overlaid is the bubble dynamics as a dashed line adapted from figure 18(a).

For a bubble in inertial collapse near a rigid boundary, the significant shear stress at the boundary occurs primarily as the shockwaves propagate and the jet spreads along the boundary. The former has a much higher amplitude, and the latter has a longer period. They both increase with decreasing Reynolds number.

ACKNOWLEDGMENTS

The computations described in this paper were performed using the University of Birmingham's BlueBEAR HPC service, which provides a High Performance Computing service to the University's research community. See http://www.birmingham.ac.uk/bear for more details. Valuable discussions were carried out with Dr. Cary Turangan, Institute of High Performance Computing, Singapore.

[1]F. Reuter, S. Lesnik, K. Ayaz-Bustami, G. Brenner, and R. Mettin, "Bubble size measurements in different acoustic cavitation structures: Filaments, clusters, and the acoustically cavitated jet," Ultrasonics sonochemistry **55**, 383–394 (2019).

[2]J. R. Blake and D. Gibson, "Cavitation bubbles near boundaries," Annual review of fluid mechanics **19**, 99–123 (1987).

[3]W. Lauterborn and T. Kurz, "Physics of bubble oscillations," Reports on progress in physics **73**, 106501 (2010).

[4]C. E. Brennen, *Cavitation and bubble dynamics* (Cambridge university press, 2014).

[5]C.-T. Hsiao, A. Jayaprakash, A. Kapahi, J.-K. Choi, and G. L. Chahine, "Modelling of material pitting from cavitation bubble collapse," Journal of Fluid Mechanics **755**, 142–175 (2014).

[6]C. C. Coussios and R. A. Roy, "Applications of acoustics and cavitation to noninvasive therapy and drug delivery," Annu. Rev. Fluid Mech. **40**, 395–420 (2008).

[7]G. Curtiss, D. Leppinen, Q. Wang, and J. Blake, "Ultrasonic cavitation near a tissue layer," Journal of Fluid Mechanics **730**, 245–272 (2013).

[8]N. Vyas, E. Pecheva, H. Dehghani, R. L. Sammons, Q. X. Wang, D. M. Leppinen, and A. D. Walmsley, "High speed imaging of cavitation around dental ultrasonic scaler tips," PLoS One **11**, e0149804 (2016).

[9]N. Vyas, H. Dehghani, R. Sammons, Q. Wang, D. Leppinen, and A. Walmsley, "Imaging and analysis of individual cavitation microbubbles around dental ultrasonic scalers," Ultrasonics **81**, 66–72 (2017).

[10]N. Vyas, K. Manmi, Q. Wang, A. J. Jadhav, M. Barigou, R. L. Sammons, S. A. Kuehne, and A. D. Walmsley, "Which parameters affect biofilm removal with acoustic cavitation? a review," Ultrasound in medicine & biology **45**, 1044–1055 (2019).

[11]Y. Yu, M. Mahmud, N. Vyas, W. R. Smith, Q. Wang, and A. D. Walmsley, "Cavitation in a periodontal pocket by an ultrasonic dental scaler: A numerical investigation," Ultrasonics Sonochemistry **90**, 106178 (2022).

[12]K. S. Suslick, "Sonochemistry," science **247**, 1439–1445 (1990).

[13]C.-D. Ohl, M. Arora, R. Ikink, N. De Jong, M. Versluis, M. Delius, and D. Lohse, "Sonoporation from jetting cavitation bubbles," Biophysical journal **91**, 4285–4295 (2006).

[14]G. L. Chahine, A. Kapahi, J.-K. Choi, and C.-T. Hsiao, "Modeling of surface cleaning by cavitation bubble dynamics and collapse," Ultrasonics

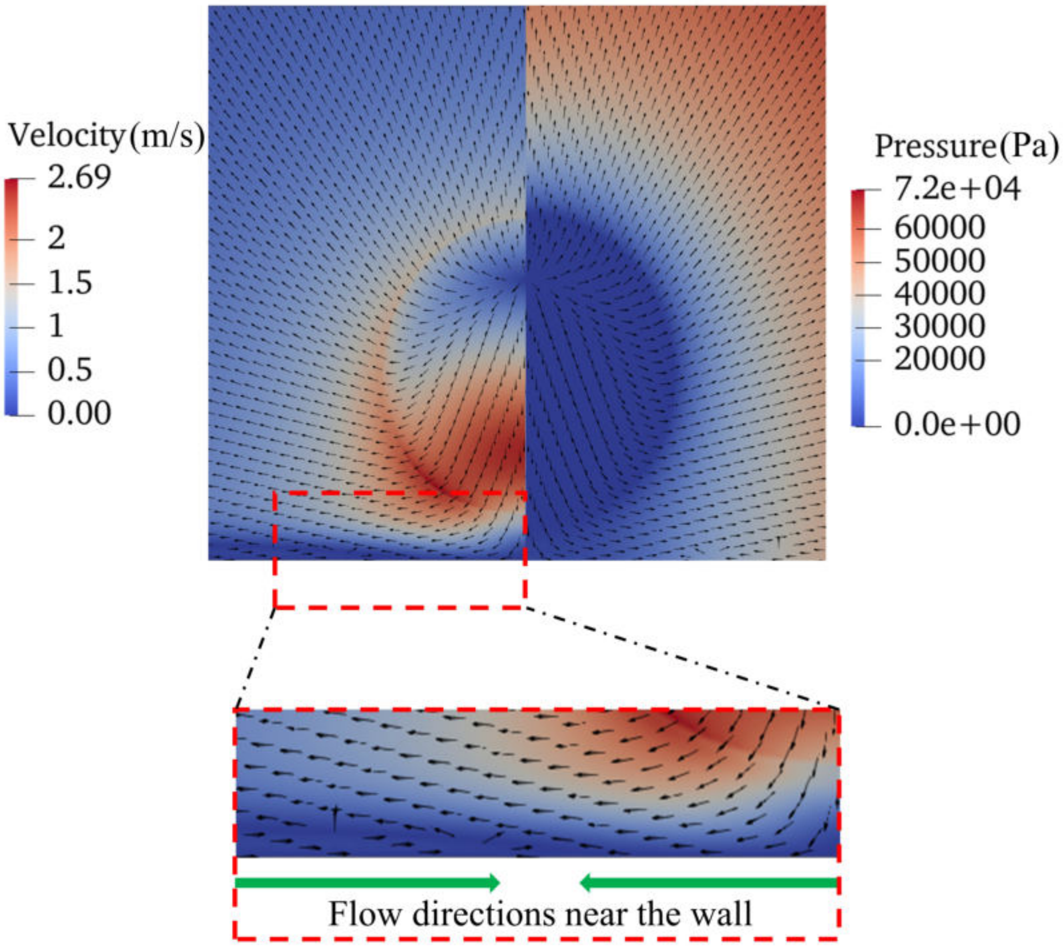

FIG. 22. Velocity vectors (black arrows), velocity contour (left), and pressure contour (right) at t = 42 μs for the case of Re = 75 in figure 13.

sonochemistry **29**, 528–549 (2016).
[15]F. Reuter, S. Lauterborn, R. Mettin, and W. Lauterborn, "Membrane cleaning with ultrasonically driven bubbles," Ultrasonics Sonochemistry **37**, 542–560 (2017).
[16]Y. Yu, W. R. Smith, Q. Wang, and A. D. Walmsley, "Numerical investigation of cavitation in periodontal pockets: Insights for enhancing cleaning efficiency," Ultrasonics Sonochemistry **100**, 106625 (2023).
[17]A. Philipp and W. Lauterborn, "Cavitation erosion by single laser-produced bubbles," Journal of Fluid Mechanics **361**, 75–116 (1998).
[18]E.-A. Brujan, K. Nahen, P. Schmidt, and A. Vogel, "Dynamics of laser-induced cavitation bubbles near elastic boundaries: influence of the elastic modulus," Journal of Fluid Mechanics **433**, 283–314 (2001).
[19]E. Brujan, G. Keen, A. Vogel, and J. Blake, "The final stage of the collapse of a cavitation bubble close to a rigid boundary," Physics of fluids **14**, 85–92 (2002).
[20]E.-A. Brujan and A. Vogel, "Stress wave emission and cavitation bubble dynamics by nanosecond optical breakdown in a tissue phantom," Journal of Fluid Mechanics **558**, 281–308 (2006).
[21]O. Lindau and W. Lauterborn, "Cinematographic observation of the collapse and rebound of a laser-produced cavitation bubble near a wall," Journal of Fluid Mechanics **479**, 327–348 (2003).
[22]E.-A. Brujan and Y. Matsumoto, "Collapse of micrometer-sized cavitation bubbles near a rigid boundary," Microfluidics and Nanofluidics **13**, 957–966 (2012).
[23]O. Supponen, D. Obreschkow, M. Tinguely, P. Kobel, N. Dorsaz, and M. Farhat, "Scaling laws for jets of single cavitation bubbles," Journal of Fluid Mechanics **802**, 263–293 (2016).
[24]O. Supponen, D. Obreschkow, P. Kobel, M. Tinguely, N. Dorsaz, and M. Farhat, "Shock waves from nonspherical cavitation bubbles," Physical Review Fluids **2**, 093601 (2017).
[25]J. Luo, W. Xu, J. Deng, Y. Zhai, and Q. Zhang, "Experimental study on the impact characteristics of cavitation bubble collapse on a wall," Water **10**, 1262 (2018).
[26]E.-A. Brujan, T. Noda, A. Ishigami, T. Ogasawara, and H. Takahira, "Dynamics of laser-induced cavitation bubbles near two perpendicular rigid walls," Journal of Fluid Mechanics **841**, 28–49 (2018).
[27]S.-M. Li, A.-M. Zhang, Q. Wang, and S. Zhang, "The jet characteristics of bubbles near mixed boundaries," Physics of Fluids **31** (2019).
[28]S. R. Gonzalez-Avila, A. C. Van Blokland, Q. Zeng, and C.-D. Ohl, "Jetting and shear stress enhancement from cavitation bubbles collapsing in a narrow gap," Journal of fluid mechanics **884**, A23 (2020).
[29]X. Ma, B. Huang, X. Zhao, Y. Wang, Q. Chang, S. Qiu, X. Fu, and G. Wang, "Comparisons of spark-charge bubble dynamics near the elastic and rigid boundaries," Ultrasonics Sonochemistry **43**, 80–90 (2018).
[30]G. Huang, M. Zhang, X. Ma, Q. Chang, C. Zheng, and B. Huang, "Dynamic behavior of a single bubble between the free surface and rigid wall," Ultrasonics sonochemistry **67**, 105147 (2020).
[31]J. Cui, Z.-P. Chen, Q. Wang, T.-R. Zhou, and C. Corbett, "Experimental studies of bubble dynamics inside a corner," Ultrasonics Sonochemistry **64**, 104951 (2020).
[32]J. Cui, T.-R. Zhou, X. Huang, and Z.-C. Li, "Experimental study of bubble dynamics in the neighbourhood of a vertical incomplete boundary," Ultrasonics Sonochemistry **75**, 105587 (2021).
[33]Y. Sun, Y. Du, Z. Yao, Q. Zhong, S. Geng, and F. Wang, "The effect of sur-

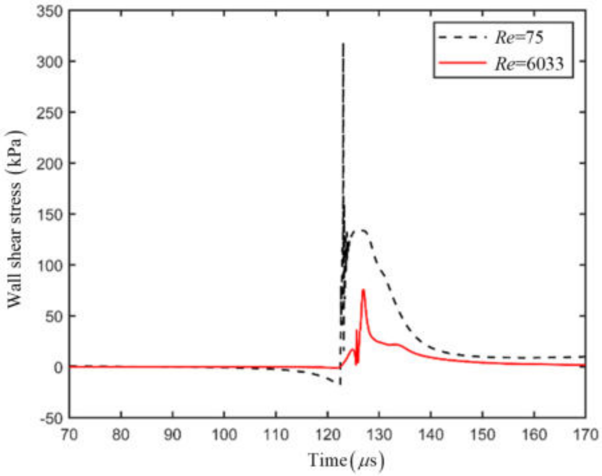

FIG. 23. The time histories of the shear stress at a point on the rigid boundary, at 180 μm from the axis of symmetry, for Re = 75, 6033 (μ_l = 0.08, 0.001 Pa $\cdot$ s, respectively). Other parameters are the same as in figure 4.

face geometry of solid wall on the collapse of a cavitation bubble," Journal of Fluids Engineering **144**, 071402 (2022).
[34]Z. Ding and S. Gracewski, "The behaviour of a gas cavity impacted by a weak or strong shock wave," Journal of Fluid Mechanics **309**, 183–209 (1996).
[35]C. Turangan, G. Ball, A. Jamaluddin, and T. Leighton, "Numerical studies of cavitation erosion on an elastic–plastic material caused by shock-induced bubble collapse," Proceedings of the Royal Society A: Mathematical, Physical and Engineering Sciences **473**, 20170315 (2017).
[36]Q. Wang, K. Yeo, B. Khoo, and K. Lam, "Vortex ring modelling of toroidal bubbles," Theoretical and Computational Fluid Dynamics **19**, 303–317 (2005).
[37]Q. Wang, "Multi-oscillations of a bubble in a compressible liquid near a rigid boundary," Journal of Fluid Mechanics **745**, 509–536 (2014).
[38]Q. Sun, E. Klaseboer, B. C. Khoo, and D. Y. Chan, "A robust and non-singular formulation of the boundary integral method for the potential problem," Engineering Analysis with Boundary Elements **43**, 117–123 (2014).
[39]Q. Wang and J. Blake, "Non-spherical bubble dynamics in a compressible liquid. part 1. travelling acoustic wave," Journal of Fluid Mechanics **659**, 191–224 (2010).
[40]Q. Wang and J. Blake, "Non-spherical bubble dynamics in a compressible liquid. part 2. acoustic standing wave," Journal of Fluid Mechanics **679**, 559–581 (2011).
[41]A. Zhang and Y.-L. Liu, "Improved three-dimensional bubble dynamics model based on boundary element method," Journal of Computational Physics **294**, 208–223 (2015).
[42]S.-M. Li, Y.-L. Liu, Q. Wang, and A. Zhang, "Dynamics of a buoyant pulsating bubble near two crossed walls," Physics of Fluids **33** (2021).
[43]A.-M. Zhang, S.-M. Li, P. Cui, S. Li, and Y.-L. Liu, "Interactions between a central bubble and a surrounding bubble cluster," Theoretical and Applied Mechanics Letters **13**, 100438 (2023).
[44]S.-M. Li, A.-M. Zhang, and N.-N. Liu, "Effect of a rigid structure on the dynamics of a bubble beneath the free surface," Theoretical and Applied Mechanics Letters **11**, 100311 (2021).
[45]T. Li, A. Zhang, S.-P. Wang, S. Li, and W.-T. Liu, "Bubble interactions and bursting behaviors near a free surface," Physics of Fluids **31** (2019).
[46]N.-N. Liu, A. Zhang, P. Cui, S.-P. Wang, and S. Li, "Interaction of two out-of-phase underwater explosion bubbles," Physics of Fluids **33** (2021).
[47]E.-A. Brujan, A.-M. Zhang, Y.-L. Liu, T. Ogasawara, and H. Takahira, "Jetting and migration of a laser-induced cavitation bubble in a rectangular channel," Journal of Fluid Mechanics **948**, A6 (2022).
[48]S. Popinet and S. Zaleski, "Bubble collapse near a solid boundary: a numerical study of the influence of viscosity," Journal of fluid mechanics **464**, 137–163 (2002).
[49]V. Minsier, J. De Wilde, and J. Proost, "Simulation of the effect of viscosity on jet penetration into a single cavitating bubble," Journal of Applied Physics **106** (2009).
[50]A. Tiwari, J. B. Freund, and C. Pantano, "A diffuse interface model with immiscibility preservation," Journal of computational physics **252**, 290–309 (2013).
[51]M. Koch, C. Lechner, F. Reuter, K. Köhler, R. Mettin, and W. Lauterborn, "Numerical modeling of laser generated cavitation bubbles with the finite volume and volume of fluid method, using openfoam," Computers & Fluids **126**, 71–90 (2016).
[52]L. Ge, A.-M. Zhang, and S.-P. Wang, "Investigation of underwater explosion near composite structures using a combined rkdg-fem approach," Journal of Computational Physics **404**, 109113 (2020).
[53]C. Lechner, M. Koch, W. Lauterborn, and R. Mettin, "Pressure and tension waves from bubble collapse near a solid boundary: A numerical approach," The Journal of the Acoustical Society of America **142**, 3649–3659 (2017).
[54]C. Lechner, W. Lauterborn, M. Koch, and R. Mettin, "Jet formation from bubbles near a solid boundary in a compressible liquid: Numerical study of distance dependence," Physical Review Fluids **5**, 093604 (2020).
[55]Y. Liu, A.-M. Zhang, Z. Tian, and S. Wang, "Investigation of free-field underwater explosion with eulerian finite element method," Ocean Engineering **166**, 182–190 (2018).
[56]N.-N. Liu, A. Zhang, Y.-L. Liu, and T. Li, "Numerical analysis of the interaction of two underwater explosion bubbles using the compressible eulerian finite-element method," Physics of Fluids **32** (2020).
[57]Q. Zeng, S. R. Gonzalez-Avila, R. Dijkink, P. Koukouvinis, M. Gavaises, and C.-D. Ohl, "Wall shear stress from jetting cavitation bubbles," Journal of Fluid Mechanics **846**, 341–355 (2018).
[58]Q. Zeng, S. R. Gonzalez-Avila, and C.-D. Ohl, "Splitting and jetting of cavitation bubbles in thin gaps," Journal of Fluid Mechanics **896**, A28 (2020).
[59]Q. Zeng, H. An, and C.-D. Ohl, "Wall shear stress from jetting cavitation bubbles: Influence of the stand-off distance and liquid viscosity," Journal of Fluid Mechanics **932**, A14 (2022).
[60]H. Xu, N. C. Eddingsaas, and K. S. Suslick, "Spatial separation of cavitating bubble populations: the nanodroplet injection model," Journal of the American Chemical Society **131**, 6060–6061 (2009).
[61]K. S. Suslick, N. C. Eddingsaas, D. J. Flannigan, S. D. Hopkins, and H. Xu, "The chemical history of a bubble," Accounts of chemical research **51**, 2169–2178 (2018).
[62]J. Dear and J. Field, "A study of the collapse of arrays of cavities," Journal of Fluid Mechanics **190**, 409–425 (1988).
[63]A. Shima, K. Takayama, Y. Tomita, and N. Ohsawa, "Mechanism of impact pressure generation from spark-generated bubble collapse near a wall," Aiaa Journal **21**, 55–59 (1983).
[64]S. W. Fong, D. Adhikari, E. Klaseboer, and B. C. Khoo, "Interactions of multiple spark-generated bubbles with phase differences," Experiments in fluids **46**, 705–724 (2009).
[65]B. Goh, S. Ohl, E. Klaseboer, and B. Khoo, "Jet orientation of a collapsing bubble near a solid wall with an attached air bubble," Physics of Fluids **26** (2014).
[66]B. H. T. Goh, S. W. Gong, S.-W. Ohl, and B. C. Khoo, "Spark-generated bubble near an elastic sphere," International Journal of Multiphase Flow **90**, 156–166 (2017).
[67]S. Gong, S. Ohl, E. Klaseboer, and B. Khoo, "Interaction of a spark-generated bubble with a two-layered composite beam," Journal of Fluids and Structures **76**, 336–348 (2018).
[68]N.-N. Liu, A. Zhang, P. Cui, S.-P. Wang, and S. Li, "Interaction of two out-of-phase underwater explosion bubbles," Physics of Fluids **33** (2021).
[69]S.-W. Ohl, E. Klaseboer, and B. C. Khoo, "Bubbles with shock waves and ultrasound: a review," Interface focus **5**, 20150019 (2015).
[70]S. R. G. Avila, C. Song, and C.-D. Ohl, "Fast transient microjets induced by hemispherical cavitation bubbles," Journal of Fluid Mechanics **767**, 31–51 (2015).
[71]H. G. Weller, G. Tabor, H. Jasak, and C. Fureby, "A tensorial approach to computational continuum mechanics using object-oriented techniques," Computers in physics **12**, 620–631 (1998).
[72]T. Li, S. Wang, S. Li, and A.-M. Zhang, "Numerical investigation of an underwater explosion bubble based on fvm and vof," Applied Ocean Research **74**, 49–58 (2018).

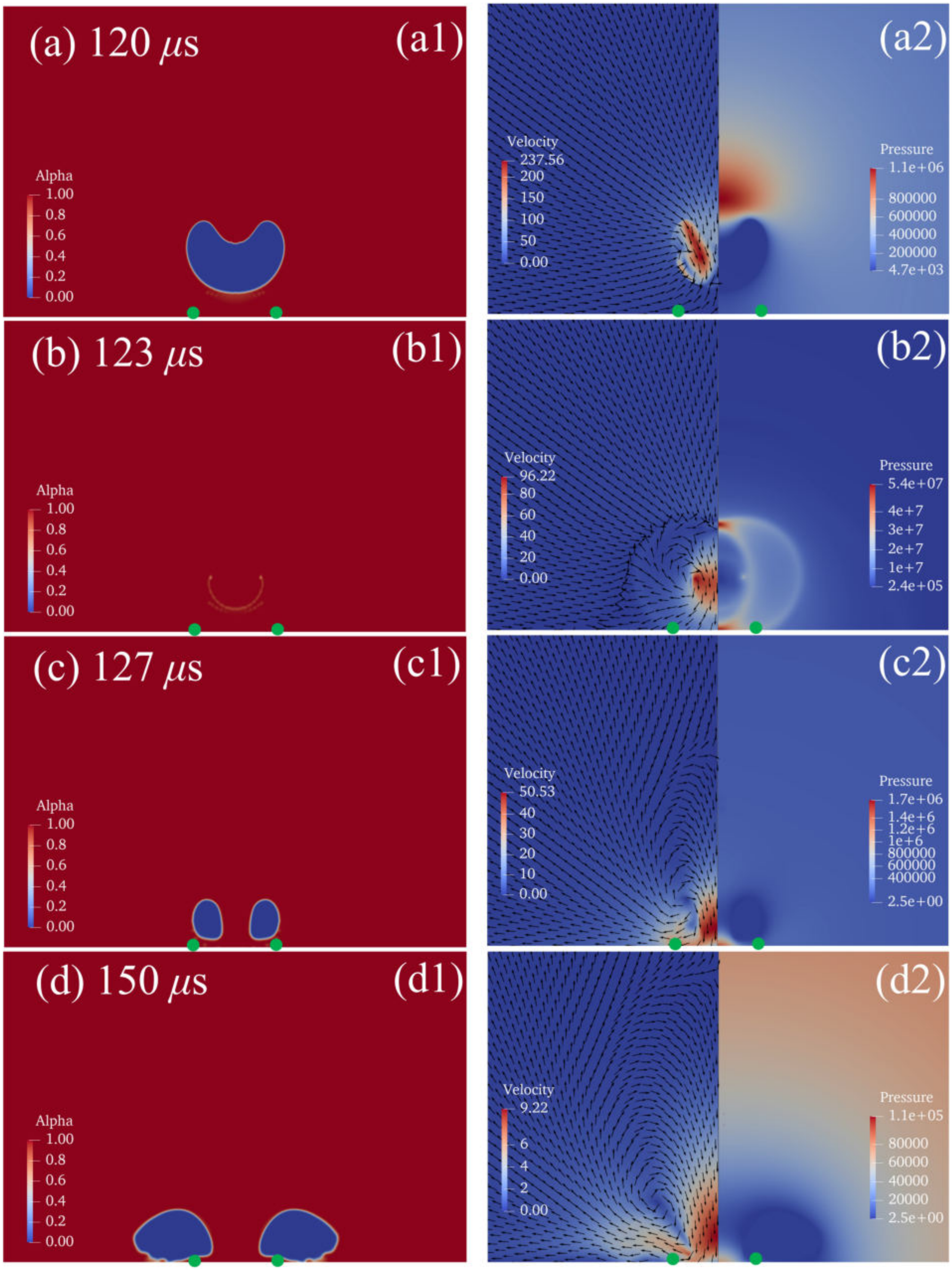

FIG. 24. Bubble shapes (frames (a1)-(d1)) and flow fields (frames (a2)-(d2)) including velocity vectors (left in frames (a2)-(d2)), velocity contours (left in frames (a2)-(d2)) and pressure contours (right in frames (a2)-(d2)) at (a) 120 μs, (b) 123 μs, (c) 127 μs, and (d) 150 μs during bubble collapse and rebound for the case of Re = 75 in figure 13.

[73]T. Li, A. Zhang, S.-P. Wang, S. Li, and W.-T. Liu, "Bubble interactions and bursting behaviors near a free surface," Physics of Fluids **31** (2019).
[74]S. R. Gonzalez-Avila, A. C. Van Blokland, Q. Zeng, and C.-D. Ohl, "Jetting and shear stress enhancement from cavitation bubbles collapsing in a narrow gap," Journal of fluid mechanics **884**, A23 (2020).
[75]H. Reese, R. Schädel, F. Reuter, and C.-D. Ohl, "Microscopic pumping of viscous liquids with single cavitation bubbles," Journal of Fluid Mechanics **944**, A17 (2022).
[76]J. M. Rosselló, H. Reese, and C.-D. Ohl, "Dynamics of pulsed laser-induced cavities on a liquid–gas interface: From a conical splash to a 'bullet' jet," Journal of Fluid Mechanics **939**, A35 (2022).
[77]J. U. Brackbill, D. B. Kothe, and C. Zemach, "A continuum method for modeling surface tension," Journal of computational physics **100**, 335–354 (1992).
[78]S. Miller, H. Jasak, D. Boger, E. Paterson, and A. Nedungadi, "A pressure-based, compressible, two-phase flow finite volume method for underwater explosions," Computers & Fluids **87**, 132–143 (2013).
[79]Y.-H. Li, "Equation of state of water and sea water," Journal of Geophysical Research **72**, 2665–2678 (1967).
[80]T. Leighton, S. Meers, and P. White, "Propagation through nonlinear time-dependent bubble clouds and the estimation of bubble populations from measured acoustic characteristics," Proceedings of the Royal Society of London. Series A: Mathematical, Physical and Engineering Sciences **460**, 2521–2550 (2004).
[81]R. Klein and L. Ting, "Far field velocity potential induced by a rapidly decaying vorticity distribution," Zeitschrift für angewandte Mathematik und Physik ZAMP **41**, 395–418 (1990).
[82]C. A. Felippa, "A family of early-time approximations for fluid-structure interaction," (1980).
[83]J. B. Keller and M. Miksis, "Bubble oscillations of large amplitude," The Journal of the Acoustical Society of America **68**, 628–633 (1980).
[84]R. Courant, K. Friedrichs, and H. Lewy, "On the partial difference equations of mathematical physics," IBM journal of Research and Development **11**, 215–234 (1967).
[85]Q. Wang, "Non-spherical bubble dynamics of underwater explosions in a compressible fluid," Physics of Fluids **25** (2013).
[86]H. Atta, "New applications in ultrasound technology," British journal of ophthalmology **83**, 1246–1249 (1999).
[87]J. C. Rogers, W. G. Szymczak, A. E. Berger, and J. M. Solomon, "Numerical solution of hydrodynamic free boundary problems," in *Free Boundary Value Problems: Proceedings of a Conference held at the Mathematisches Forschungsinstitut, Oberwolfach, July 9–15, 1989* (Springer, 1990) pp. 241–266.
[88]W. G. Szymczak, J. C. Rogers, J. M. Solomon, and A. E. Bergert, "A numerical algorithm for hydrodynamic free boundary problems," Journal of Computational Physics **106**, 319–336 (1993).
[89]Q. Wang, "Local energy of a bubble system and its loss due to acoustic radiation," Journal of Fluid Mechanics **797**, 201–230 (2016).
[90]D. Akhmetov, "Loss of energy during the motion of a vortex ring." Journal of Applied Mechanics & Technical Physics **49** (2008).
[91]T. Pedley, "The toroidal bubble," Journal of Fluid Mechanics **32**, 97–112 (1968).
[92]T. S. Lundgren and N. N. Mansour, "Vortex ring bubbles," Journal of Fluid Mechanics **224**, 177–196 (1991).
[93]S. Zhang, J. H. Duncan, and G. L. Chahine, "The final stage of the collapse of a cavitation bubble near a rigid wall," Journal of Fluid Mechanics **257**, 147–181 (1993).
[94]Q. Wang, K. Yeo, B. Khoo, and K. Lam, "Strong interaction between a buoyancy bubble and a free surface," Theoretical and Computational Fluid Dynamics **8**, 73–88 (1996).
[95]A. Zhang and Y.-L. Liu, "Improved three-dimensional bubble dynamics model based on boundary element method," Journal of Computational Physics **294**, 208–223 (2015).
[96]Y. Tomita and A. Shima, "Mechanisms of impulsive pressure generation and damage pit formation by bubble collapse," Journal of Fluid Mechanics **169**, 535–564 (1986).